The energy cascade in near-field non-homogeneous non-isotropic turbulence

R. Gomes-Fernandes[1] B. Ganapathisubramani [2] and J. C. Vassilicos[1]

[1]Department of Aeronautics, Imperial College London, London SW7 2AZ, UK

[2]Aerodynamics & Flight Mechanics Research Group, University of Southampton, Southampton SO17 1BJ, UK

(Received ?; revised ?; accepted ?. - To be entered by editorial office)

We perform Particle Image Velocimetry (PIV) measurements of various terms of the non-homogeneous Kármán-Howarth-Monin equation in the most inhomogeneous and anisotropic region of grid-generated turbulence, the production region which lies between the grid and the peak of turbulence intensity. We use a well-documented fractal grid which is known to magnify the streamwise extent of the production region and abate its turbulence activity. On the centreline around the centre of that region the two-point advection and transport terms are dominant and the production is significant too. It is therefore impossible to apply usual Kolmogorov arguments based on the Kármán-Howarth-Monin equation and resulting dimensional considerations to deduce interscale flux and spectral properties. The interscale energy transfers at this location turn out to be highly anisotropic and consist of a combined forward and inverse cascade in different directions which, when averaged over directions, give an interscale energy flux which is negative (hence forward cascade on average) and not too far from linear in r, the modulus of the separation vector $\mathbf{r}$ between two points. The energy spectrum of the streamwise fluctuating component exhibits a well-defined -5/3 power law over one decade even though the streamwise direction is at a small angle to the inverse cascading direction.

1. Introduction

The mathematical formulation of the Richardson-Kolmogorov cascade (Richardson 1922; Kolmogorov 1941*b*,*c*,*a*; Batchelor 1953) is based on the evolution equation for the second order structure function $\overline{\delta q^2} = \overline{(\delta u_i)^2}$ (with an implicit summation over the index i) where the overbar denotes an average over realisations or, in practice in this paper, over time. In this structure function, $\delta u_i \equiv u_i - u_i'$ where u_i ($i = 1, 2, 3$) is a fluctuating velocity component at a location $\mathbf{x} = \mathbf{X} + \mathbf{r}/2$ in the turbulent flow and u_i' is the same fluctuating velocity component at a different location, namely $\mathbf{x}' = \mathbf{X} - \mathbf{r}/2$. This evolution equation is usually refered to as the Kármán-Howarth or the Kármán-Howarth-Monin equation and it can be written down without assumptions of statistical homogeneity and isotropy (see Deissler 1961; Hill 2002; Marati *et al.* 2004; Danaila *et al.* 2012; Valente & Vassilicos 2015) in which case $\overline{\delta q^2}$ is a function of both the centroid $\mathbf{X}$ and the separation vector $\mathbf{r}$. The starting point is the Navier-Stokes equation for incompressible flow where the velocity and pressure fields have been decomposed into mean (in upper case notation) and fluctuating (in lower case notation) fields, i.e.

$$\frac{\partial \left(U_i + u_i\right)}{\partial t} + \left(U_k + u_k\right) \frac{\partial U_i + u_i}{\partial x_k} = -\frac{1}{\rho} \frac{\partial}{\partial x_i} \left(P + p\right) + \nu \nabla^2 \left(U_k + u_k\right) \qquad (1.1)$$

(ρ and ν are, respectively, the mass density and kinematic viscosity of the fluid). By incompressibility, $\frac{\partial}{\partial x_i}U_i = \frac{\partial}{\partial x_i}u_i = 0$. Using the Navier-Stokes and incompressibility equations at both locations $\mathbf{x}$ and $\mathbf{x}'$ and operating a change of variables from ($\mathbf{x}$,$\mathbf{x}$') to ($\mathbf{X}$,$\mathbf{r}$) one derives the following Kármán-Howarth-Monin equation by standard mathematical manipulations (see Hill 2002; Marati *et al.* 2004; Danaila *et al.* 2012; Valente & Vassilicos 2015):

$$\frac{\partial\overline{\delta q^2}}{\partial t} + \left(\frac{U_k + U'_k}{2}\right)\frac{\partial\overline{\delta q^2}}{\partial X_k} + \frac{\partial\overline{\delta u_k \delta q^2}}{\partial r_k} + \frac{\partial \delta U_k \overline{\delta q^2}}{\partial r_k} = 4\mathcal{P} + 4\mathcal{T} + 4\mathcal{T}_p + 4\mathcal{D}_\nu + 4\mathcal{D}_{X,\nu} - 4\epsilon^* \tag{1.2}$$

where $\delta U_k \equiv U_k - U'_k$, $\delta p \equiv p - p'$ and:

- $4\mathcal{P}(\mathbf{X},\mathbf{r}) \equiv -2\overline{u_k \delta u_i}\partial U_i/\partial x_k + 2\overline{u'_k \delta u_i}\partial U'_i/\partial x'_k$ represents the turbulent production term which is kept in its expression as a function of $\mathbf{x} = \mathbf{X} + \mathbf{r}/2$ and $\mathbf{x}' = \mathbf{X} - \mathbf{r}/2$;

- $4\mathcal{T}(\mathbf{X},\mathbf{r}) \equiv -\partial/\partial X_k(\overline{(u_k + u'_k)\delta q^2}/2)$ represents turbulent transport along $\mathbf{X}$ of $\delta q^2 \equiv (\delta u_i)^2$ which is a function of $\mathbf{X}$ and $\mathbf{r}$;

- $4\mathcal{T}_p(\mathbf{X},\mathbf{r}) \equiv -2/\rho\partial\overline{\delta u_k \delta p}/\partial X_k$ represents turbulent transport along $\mathbf{X}$ of $\delta p(\mathbf{X},\mathbf{r})$;

- $4\mathcal{D}_\nu(\mathbf{X},\mathbf{r}) \equiv 2\nu\partial^2\overline{\delta q^2}/\partial r_k^2$ is the viscous diffusion in the space of separation vectors $\mathbf{r}$ (note that $\mathcal{D}_\nu(\mathbf{X},\mathbf{r}) = \epsilon(\mathbf{X})$ in the limit $|\mathbf{r}| \equiv r \to 0$);

- $4\mathcal{D}_{X,\nu}(\mathbf{X},\mathbf{r}) \equiv \nu/2\partial^2\overline{\delta q^2}/\partial X_k^2$ is the viscous diffusion in physical space (i.e. along $\mathbf{X}$);

- $4\epsilon^*(\mathbf{X},\mathbf{r}) \equiv 2\nu\overline{(\partial u_i/\partial x_k)^2} + 2\nu\overline{(\partial u'_i/\partial x'_k)^2}$ is the sum of two times the turbulent kinetic energy dissipation evaluated at each location with $\epsilon^* = (\epsilon + \epsilon')/2$.

By assuming that at small enough separations $r \equiv |\mathbf{r}|$ the turbulence is locally statistically homogeneous in the frame moving with the mean flow, all the terms on the right hand side of equation 1.2 vanish except $4\mathcal{D}_\nu$ and $4\epsilon^*$. Furthermore, the viscous diffusion term $4\mathcal{D}_\nu$ can reasonably be neglected at high enough Reynolds numbers for a given r which is larger than length-scales where viscous diffusion is significant. With these simplifying assumptions, equation 1.2 becomes

$$\frac{\partial\overline{\delta q^2}}{\partial t} + \left(\frac{U_k + U'_k}{2}\right)\frac{\partial\overline{\delta q^2}}{\partial X_k} + \frac{\partial\overline{\delta u_k \delta q^2}}{\partial r_k} = -4\epsilon\ . \tag{1.3}$$

The only remaining terms are:

- $4\mathcal{A}_t(\mathbf{X},\mathbf{r}) \equiv \partial\overline{\delta q^2}/\partial t$ (which cancels when the flow is statistically stationary and the average can be taken over time);

- $4\mathcal{A}(\mathbf{X},\mathbf{r}) \equiv (U_k + U'_k)/2\partial\overline{\delta q^2}/\partial X_k$ which is the advection of $\overline{\delta q^2}(\mathbf{X},\mathbf{r})$ by the mean flow (and which equals $U_k\partial\overline{\delta q^2}/\partial X_k$ when there is statistical homogeneity);

- $4\Pi(\mathbf{X},\mathbf{r}) \equiv \partial\overline{\delta u_k \delta q^2}/\partial r_k$ which is the non-linear energy transfer term. The divergence of the flux $\overline{\delta u_k \delta q^2}$ transfers fluctuating energy from spherical shells centred at $\mathbf{X}$ with radius $r = |\mathbf{r}|$ either to spherical shells centred at the same $\mathbf{X}$ but with different

radius or within the same spherical shell but to a different orientation $\mathbf{r}/r$;

- $4\epsilon^*(\mathbf{X},\mathbf{r}) \equiv 4(\epsilon+\epsilon')/2$ which equals 4ϵ when there is statistical homogeneity.

Note that statistical homogeneity has also allowed us to discard $4\Pi_U(\mathbf{X},\mathbf{r}) = \partial\delta U_k\overline{\delta q^2}/\partial r_k$ which is the linear energy transfer by the mean flow and which has a similar interpretation as $4\Pi(\mathbf{X},\mathbf{r})$ but in relation to the flux $U_k\overline{\delta q^2}$.

The critical equilibrium assumption made by Kolmogorov (1941*b*,*c*,*a*) is that, at high enough Reynolds number, the time scales characterising the evolution of $\overline{\delta q^2}$ at small enough scales r are much smaller than the time scale characterising homogeneous turbulence decay, thus implying

$$\frac{\partial\overline{\delta q^2}}{\partial t} + \left(\frac{U_k + U_k'}{2}\right)\frac{\partial\overline{\delta q^2}}{\partial X_k} \approx 0\ . \tag{1.4}$$

Kolmogorov's assumption leads directly to an equilibrium between nonlinear energy transfer and dissipation which is the crux of the Richardson-Kolmogorov cascade, namely

$$\frac{\partial\overline{\delta u_k \delta q^2}}{\partial r_k} \approx -4\epsilon\ . \tag{1.5}$$

Integrating both sides of this balance over a sphere of radius $|\mathbf{r}| = r$ as in Nie & Tanveer (1999) and making use of the Gauss divergence theorem we get

$$\int \overline{\delta\mathbf{u}\delta q^2}.\frac{\mathbf{r}}{r}\,d\Omega \approx \int -4\epsilon\,dV\ = -\frac{16\pi}{3}\epsilon r\ , \tag{1.6}$$

where $d\Omega$ and dV are differentials of a solid angle and a volume, respectively. If the assumption of small-scale isotropy is made, i.e. that $\overline{\delta\mathbf{u}\delta q^2}.\frac{\mathbf{r}}{l}$ is independent of the orientation of the unit vector $\mathbf{r}/r$, then this integral yields the expression

$$\overline{\delta\mathbf{u}_{||}\delta q^2} \approx -\frac{4}{3}\epsilon r\ , \tag{1.7}$$

where $\delta\mathbf{u}_{||} \equiv \delta\mathbf{u}.\mathbf{r}/r$. This expression and the equilibrium balance equation 1.5 are the central properties of the Richardson-Kolmogorov cascade and are valid over the so-called inertial range of scales r which are neither too small for viscous effects to be significant nor too large to be comparable with the size of the largest turbulent eddies where Kolmogorov's assumption 1.4 will certainly break down. The minus sign in equation 1.7 indicates that the energy cascades from large to small scales and the independence of the equilibrium balance 1.5 on $\mathbf{r}$ (as long as r is in the inertial range) implies a self-similar cascade, i.e. one where the divergence of the flux $\overline{\delta u_k\delta q^2}$ is independent of $\mathbf{r}$ and proportional to the dissipation rate ϵ. This last concept then sets the foundations for the dimensional analysis which leads to the celebrated $2/3$ and $-5/3$ respective scalings of the second order structure function and the energy spectrum of small-scale turbulence (Kolmogorov 1941*b*,*c*,*a*; Batchelor 1953).

In the present paper we explore these ideas in a non-homogeneous turbulence where equation 1.3 is not valid and one therefore needs to revert to the full non-homogeneous Kármán-Howarth-Monin equation 1.2. However we explore these ideas in a highly inhomogeneous part of a turbulent flow where Kolmogorov's $2/3$ power law has been reported to exist, namely in the production region of a turbulent flow generated by a fractal square grid obstructing a free stream (Laizet *et al.* 2013; Gomes-Fernandes *et al.* 2014). The production region is a region near the turbulence-generating grid where the turbulence does

Grid	N	t_r	R_L	t_0 (mm)	t_{min} (mm)	L_0 (mm)	$L_{min}(mm)$	σ (%)
SFG17	4	17	0.5	23.5	1.4	303.3	37.9	25

TABLE 1. Space-filling fractal square grid SFG17 geometric details. $t_{min} = t_3$, $L_{min} = L_3$

not decay with streamwise distance at all spanwise locations but in fact grows with streamwise distance, in particular along the centreline where it grows for the longest streamwise extent. The advantage of a fractal square grid over a regular one, for example, is that the fractal square grid magnifies the spatial extent of the production region and abates its activity there thus making measurements possible or at the very least less difficult, see Mazellier & Vassilicos (2010); Laizet & Vassilicos (2011, 2012, 2015); Nagata *et al.* (2013) who have documented the inhomogeneous and anisotropic nature of the production region downstream of a fractal grid and in particular Laizet & Vassilicos (2012, 2015) who have made comparisons with regular grids.

In section 2 we decribe our experimental facility and measurement locations and technique and in section 3 we present our first results concerning energy spectra and the third order structure function $\overline{\delta\mathbf{u}_{||}\delta q^2}$. In section 4 we describe how we reduce from our measurements the different terms in equation 1.2, what assumptions we make and what terms we are unable to obtain. In sections 5 and 6 we report on these terms and we conclude in section 7.

2. Experimental details

2.1. *Experimental facility and grid geometry details*

Experiments are carried out in a recirculating water tunnel whose schematic is shown in figure 1. The test section has a cross sectional area of 0.6×0.6 m^2 and is 9 m long. Transparent perspex sheets are installed as a roof to prevent any gravitational waves to interfere with the flow. The free-stream turbulence intensity is 2.8% for the streamwise fluctuating velocity u and 4.4% for the spanwise fluctuating velocity v. For more details on the experimental facility see Gomes-Fernandes *et al.* (2012, 2014).

In the present work, the space-filling fractal square grid SFG17 is used. This fractal grid was introduced by Hurst & Vassilicos (2007) and then used for turbulence studies by Seoud & Vassilicos (2007), Mazellier & Vassilicos (2010), Valente & Vassilicos (2011), Gomes-Fernandes *et al.* (2012), Discetti *et al.* (2013), Nagata *et al.* (2013), Valente & Vassilicos (2014) and Gomes-Fernandes *et al.* (2014). There is therefore a wealth of data by now on the turbulence generated by this grid. Figure 2 shows a schematic of the SFG17. It has four "fractal iterations" (N), a thickness ratio (t_r) of 17 (t_r is the ratio between the thickness of the thickest bar t_0 and that of the thinnest bar t_{min}) and a blockage ratio of 25%. L_0 is the length of the thickest bars. The ratio between the lengths of two consecutive iterations is $R_L = L_{i+1}/L_i$ (i from 0 to $N-1$) is 1/2. Defined in a similar way, the ratio between the thickness of two consecutive iterations $R_t = t_{i+1}/t_i$ is $t_r^{1/(N-1)}$. The grid thickness in the streamwise direction is 5 mm. Full geometrical details are found in table 1.

The inlet velocity U_∞ was set to 0.48 ms^{-1}, case A of Gomes-Fernandes *et al.* (2012). Table 2 shows a summary of the inlet velocities and global Reynolds numbers for the present study. Global Reynolds number is denoted this way given that it does not depend on space and time as it is fully determined by the inlet conditions.

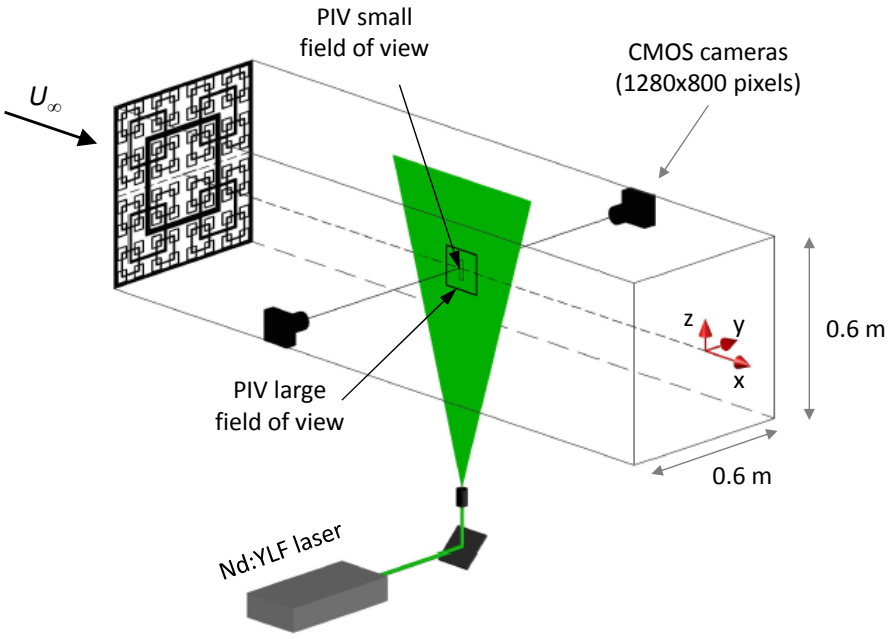

FIGURE 1. Schematic of the water tunnel and PIV setup.

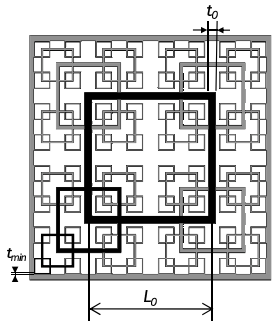

FIGURE 2. Schematic of the SFG17 after Gomes-Fernandes *et al.* (2012). The $N = 4$ "fractal iterations" are highlighted in black and further details on the geometrical parameters are found in table 1.

U_∞	Re_0	Re_{L_0}
0.48	11200	144900

TABLE 2. Experimental conditions: free-stream velocities and global Reynolds numbers. Re_0 and Re_{L_0} are the Reynolds numbers based on the thickness t_0 and on the length L_0, respectively (see figure 2): $Re_0 = U_\infty t_0/\nu$ and $Re_{L_0} = U_\infty L_0/\nu$

2.2. *Measurement locations*

Before describing our measurement technique, we need to explain how we chose our measurement locations. Figure 3 shows the behaviour of turbulence intensity of the streamwise velocity fluctuation (u'/U_∞) generated by space-filling fractal square grids from two different experiments (Mazellier & Vassilicos 2010; Gomes-Fernandes *et al.* 2012). The streamwise distance x is normalized by $x_*^{peak} \propto L_0^2/(\alpha C_d t_0)$ where α is a parameter that takes into account the incoming free-stream turbulence and C_d is the drag coefficient of the thickest bar if assumed of infinite length. This scale x_*^{peak} is an estimator of the turbulence intensity peak location and an improvement on the wake interaction length scale introduced by Mazellier & Vassilicos (2010). Note that in the present case $x_*^{peak} = 1.36$m which allows us to have a considerable physical space to perform PIV in the production region as opposed to what happens with usual regular grids where $x_*^{peak} \approx 3M$ with M, the mesh size, being of the order of 0.025m (see Jayesh & Warhaft 1992). In addition, the fractal grid generates a lower level of turbulence intensity in this region when compared to the regular ones making it easier to capture the smallest scales of the flow while maintaining a good dynamic range in space. The turbulence intensity can be a priori estimated as being about $1.6\beta^{-1}(C_d t_0/x_*^{peak})^{1/2}$ at $x = x_*^{peak}$ (β is another parameter that takes into account the incoming free-stream turbulence), see figure 3. More explanations for these scalings can be found in Gomes-Fernandes *et al.* (2012).

All our measurements are located in the production region which lies between the grid and a streamwise distance $x = x_*^{peak}$ from the grid. Specifically, our measurement stations are at x/x_*^{peak}=0.20, 0.44 and 0.57 along the centreline. An additional measurement is made very close to the fractal grid, downstream of the thickest bar at $x/x_*^{peak} = 0.08$ with the PIV field of view centered as in figure 4 to measure the frequency of the Kármán vortex shedding.

2.3. *Experimental technique*

We use planar, two-component Particle Image Velocimetry (PIV) to measure the velocity field in the aforementioned stations. Figure 1 shows a schematic of the PIV system which consists of a Nd:YLF laser (Litron LDY304 with 30 mJ/pulse at 1kHz) with an output wavelength of 527 nm and a pair of CMOS cameras (Phantom v210). The cameras face the same interrogation area but with different magnifications resulting in two different fields of view: small and large. Both fields of view are in the xz plane and include the centreline (see figure 1).

The laser light sheet is obtained by bending the beam 90° with a mirror, passing it through a spherical lens to converge the beam into a minimum thickness of around 1.2 mm (measured in Gomes-Fernandes *et al.* (2014)) and through a cylindrical lens to create the light sheet seen in figure 1.

For the Large Field of View (LFV), the cameras are operated at a resolution of 1280 x 800 pixels and are synchronized with the laser at a frequency of 500 Hz. They were fitted with a Nikon 60 mm lenses with a f# of 5.6. Five runs of 8216 vector fields were acquired using the large field of view at x/x_*^{peak}=0.20, 0.44 and 0.57. A summary of the resolution related to the LFV is shown in table 3 where the Kolmogorov scale $\eta = (\nu^3/\epsilon)^{1/4}$ with ν being the water's kinematic viscosity and ϵ the turbulent kinetic energy dissipation. As for the Small Field of View (SFV), the cameras operate at a resolution and frequency shown in table 4. Ten runs of 102709 vector fields were acquired using this field of view at x/x_*^{peak}=0.20, 0.44 and 0.57. The cameras were fitted with a Sigma 180 mm Macro lens with a f# of 8. For the station downstream of the thickest bar a Sigma 180 mm Macro lens is used with a f# of 5.6. The magnification is set to achieve a resolution close to

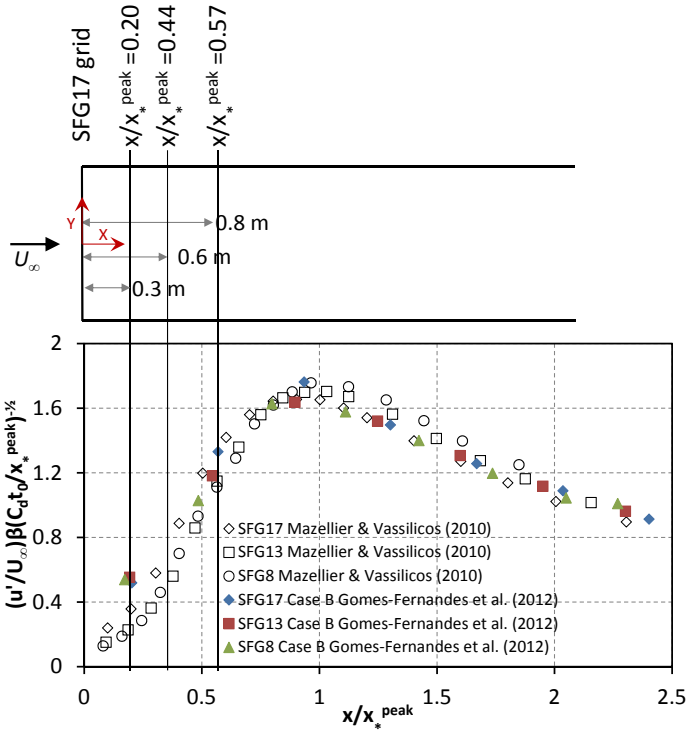

FIGURE 3. Streamwise evolution of the centreline turbulence intensity generated by space-filling square fractal grids after Gomes-Fernandes *et al.* (2012, pp. 325) and a plan view of the measurement locations for the present study.

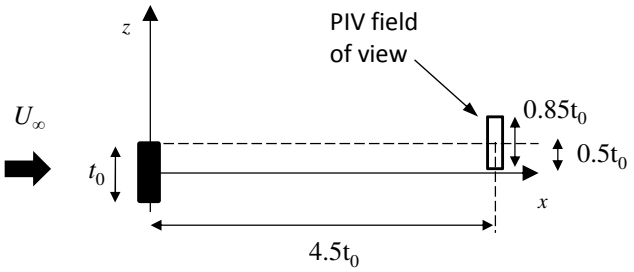

FIGURE 4. Location of measurements behind one of the biggest bars at $x/x_*^{peak} = 0.08$ from the grid and centered at a $0.5t_0$ transverse (z) distance from the bar's centre.

$t_0/10$ to capture the secondary instabilities according to the DNS of Dong *et al.* (2006) at a similar Reynolds number compared to the present experiment (see table 2). Three runs of 513600 vector fields were acquired at this station.

Distortion and other aberrations introduced by the lenses and water/glass interface

Station	Camera resolution (pixels)	Frequency of acquisition (Hz)	Experimental resolution	Vector count
$x/x_*^{peak} = 0.20$	1280×800	500	7.0η	160×100
$x/x_*^{peak} = 0.44$	1280×800	500	8.4η	160×100
$x/x_*^{peak} = 0.57$	1280×800	500	10.5η	160×100

TABLE 3. Experimental resolution computed with the large field of view. The resolution is based on the Kolmogorov length scale at the centreline in the respective location.

Station	Camera resolution (pixels)	Frequency of acquisition (Hz)	Experimental resolution	Vector count
$x/x_*^{peak} = 0.08$	256×64	1000	N/A	16×3
$x/x_*^{peak} = 0.20$	128×128	2000	4.3η	16×16
$x/x_*^{peak} = 0.44$	1280×64	2000	5.0η	80×3
$x/x_*^{peak} = 0.57$	1280×64	2000	6.1η	80×3

TABLE 4. Experimental resolution computed with the small field of view. The resolution is based on the Kolmogorov length scale at the centreline in the respective location when applicable.

were corrected using a calibration target with a fixed grid. A third-order polynomial function after Soloff *et al.* (1997) is fitted to map the vectors from image to object plane.

The flow is seeded with polyamide 12 powder with a nominal size of 7 μm and a specific gravity of around 1.1. The response time (τ_P) of the seeding particles is estimated to be 0.24 μs. The Stokes number $St = \tau_P/\tau_F$ is estimated using the Kolmogorov time scale $\tau_\eta = \sqrt{\nu/\epsilon}$ as the characteristic time scale (τ_F). In our case $St = 5 \times 10^{-6}$ which is substantially smaller than unity.

The images were acquired in single frame mode. Frame 1 was correlated with frame 2 to get the first velocity field, frames 3 and 4 to get the second one and so forth. The final interrogation window size was 32×32 pixels with 50% overlap for the small field of view and 16×16 pixels with 50% overlap for the large field of view. The number of total vectors for the large and small field of views, respectively, are 3×80 and 160×100 in the $x \times y$ directions. The number of spurious vectors was less than 1% for both field of views. The time between frames allow a 8 pixel displacement on average.

Figure 5 shows examples of the instantaneous fluctuating velocity field and of the mean velocity field at $x/x_*^{peak} = 0.44$ from the small and large fields of view, respectively.

Using the small field of view, the Taylor microscale $\lambda = \sqrt{\langle u^2 \rangle \,/\, \langle (\partial u/\partial x)^2 \rangle}$ (where $u \equiv u_1$) is computed at x/x_*^{peak}=0.44 and 0.57 and it takes values of 7.2 mm and 10.3 mm, respectively, at the centrelines. The values of λ do not change significantly across the z direction amounting to values between 6.5-7.3 mm and 9.2-11.2 mm for x/x_*^{peak}=0.44 and 0.57, respectively. Table 5 shows the Re_λ for the three stations measured in the production region.

3. Energy spectra and third order structure function

3.1. *Energy spectra and data filtering*

Figure 6 shows the one-dimensional longitudinal energy spectra E_{11} in the frequency domain evaluated at x/x_*^{peak}=0.44 for $z = y = 0$, i.e., at the centreline, using raw and filtered data from the small field of view. In the horizontal axis we show the frequency

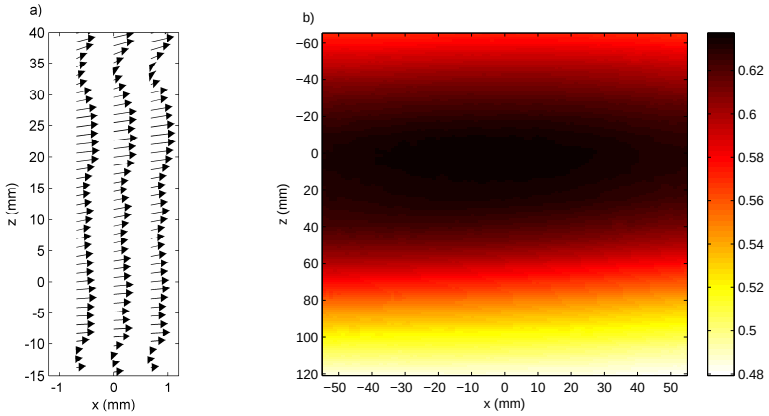

FIGURE 5. a) Instantaneous fluctuating velocity field at $x/x_*^{peak} = 0.44$ obtained from the small field of view. Only half the vector count is included in the z direction. b) Mean velocity field at $x/x_*^{peak} = 0.44$ obtained from the large field of view.

Station	Re_λ
$x/x_*^{peak} = 0.20$	102
$x/x_*^{peak} = 0.44$	190
$x/x_*^{peak} = 0.57$	268

TABLE 5. Reynolds numbers $Re_\lambda = u'\lambda/\nu$ where u' is the r.m.s. of the streamwise velocity fluctuation, $\lambda = \sqrt{\langle u^2 \rangle \,/\, \langle (\partial u/\partial x)^2 \rangle}$ is the Taylor microscale and ν is the kinematic viscosity.

normalised by the lateral thickness of the largest bars, t_0 (see table 1), and the freestream velocity, U_∞ (see table 2). There is a one decade power law with an approximate -5/3 exponent in this location and even more clearly at x/x_*^{peak}=0.57 (see figures 8a and 8b) even though Gomes-Fernandes *et al.* (2014) reported that at $x/x_*^{peak} = 0.57$ on the centreline, vortex stretching only marginally dominates over vortex compression whereas in the decay region ($x/x_*^{peak} = 2.04$) and in various reference cases reported in the literature (such as regular grid turbulence and atmospheric surface layer), vortex stretching dominates over vortex compression very significantly.

At $ft_0/U_\infty \gtrsim 10$ the spectra display a noise floor. In order to reduce the effect of noise in the velocity gradients, a filter is applied to the data. The filter consists of a Gaussian kernel applied to the temporal data with a full width of the experimental resolution (via Taylor's hypothesis) at $1/e^2$. The result is shown in figure 6 where the effect of noise is greatly reduced. The filter is also applied to the w component of the measured fluctuating velocity and displays the same behaviour as the u component.

The peak appearing approximately around $ft_0/U_\infty = 0.13$ (see figure 6) is related to the initial conditions, more specifically to the Kármán vortex shedding of the largest bars. Figure 7a shows the one-dimensional longitudinal energy spectra downstream of the largest bar (see figure 4), centred in the y direction at $x/x_*^{peak} = 0.08$, confirming that the peak at $St_K = 0.13$ is related to the Kármán vortex shedding. It is also worth noting that the power law exponent of the inertial range is close to 2 which is consistent with the vortex sheet structure of the flow at such close distance from the grid. As for

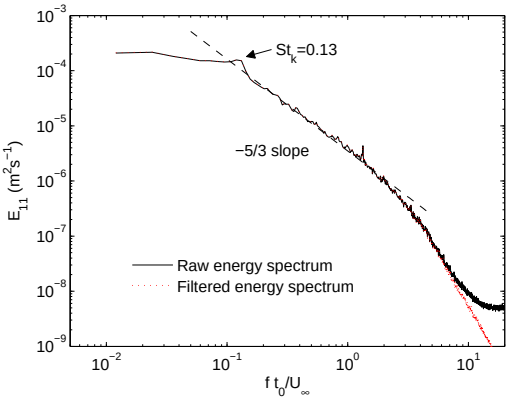

FIGURE 6. One-dimensional longitudinal energy spectra E_{11} at the centreline position $x/x_*^{peak} = 0.44$ from raw and filtered PIV data. The horizontal axis represents the frequencies normalised by the lateral thickness of the largest bars, t_0, and the freestream velocity, U_∞.

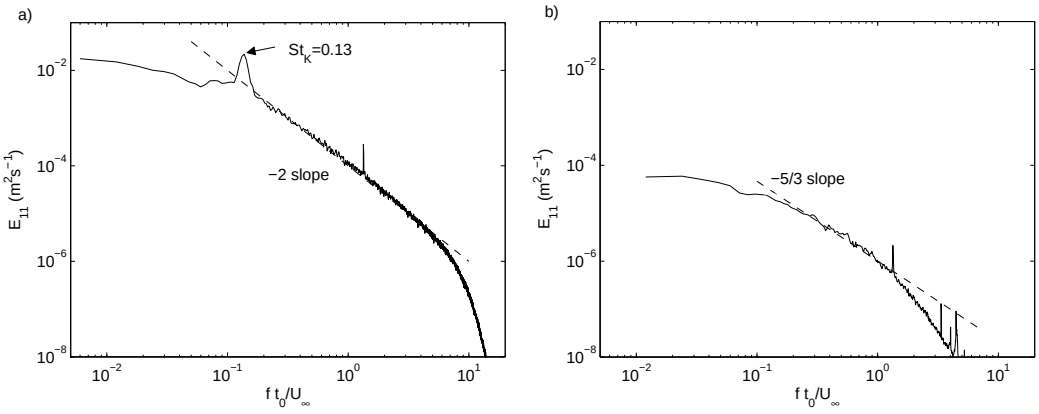

FIGURE 7. a) One-dimensional longitudinal energy spectra E_{11} at the off-centreline position $x/x_*^{peak} = 0.08$ shown in figure 4) downstream of one of the largest bars. b) One-dimensional longitudinal energy spectra E_{11} at $x/x_*^{peak} = 0.20$ on the centreline without the grid in place. The horizontal axis represents the frequencies normalised by the lateral thickness of the largest bars, t_0, and the freestream velocity, U_∞.

the second peak seen at $ft_0/U_\infty = 1.3$ in figure 6, the same peak appears in the spectra at $x/x_*^{peak} = 0.20$ when the grid is not in place (see figure 7b), thus suggesting that its origin is not in the turbulence generated by the fractal grid.

The spatial evolution of the one-dimensional spectra from station $x/x_*^{peak} = 0.20$, to $x/x_*^{peak} = 0.44$ and eventually $x/x_*^{peak} = 0.57$ is shown in figures 8a and 8b and corresponds to an evolution from $Re_\lambda = 102$, to $Re_\lambda = 190$ and eventually $Re_\lambda = 268$ (table 5). At $x/x_*^{peak} = 0.20$ the Kármán vortex shedding's signature is not present in this centreline spectrum but it does appear at $x/x_*^{peak} = 0.44$. At $x/x_*^{peak} = 0.44$ the spectrum has already a decade of scaling with exponent close to -5/3 (see the compensated spectra

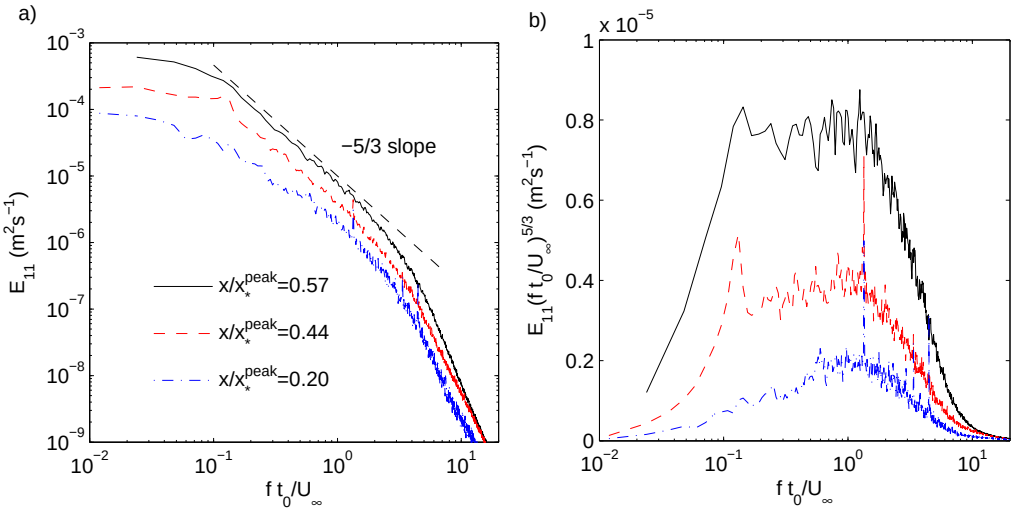

FIGURE 8. a) Spatial evolution of the one-dimensional spectra at centreline positions $x/x_*^{peak} = 0.20$, 0.44 and 0.57 and b) the same data compensated by $(ft_0/U_\infty)^{5/3}$ in linear-logarithmic axes. The horizontal axis represents the frequencies normalised by the lateral thickness of the largest bars, t_0, and the freestream velocity, U_∞.

in figure 8b). At $x/x_*^{peak} = 0.57$ the existence of a decade of -5/3 scaling is very clear even though we are at the heart of the production region where the turbulence is highly inhomogeneous and the turbulence intensity is still rising with streamwise distance from the grid.

3.2. *Third order structure function and statistical convergence*

The third order structure function $\overline{\delta u_{||} \delta q^2}$ can be calculated with $\mathbf{r}$ along the streamwise direction, i.e. $\mathbf{r} = (r_1, 0, 0)$, by making use of the Taylor hypothesis in this direction. We established the validity of this hypothesis at x/x_*^{peak}=0.44 and 0.57 and we present details of this validation in appendix A. In figure 9 we plot this third order structure function which we have calculated by assuming that $\overline{\delta u \delta q^2} \approx \overline{\delta u^3} + 2\overline{\delta u \delta w^2}$ (where $u \equiv u_1$, $v \equiv u_2$ and $w \equiv u_3$). In this figure, $\overline{\delta u_{||} \delta q^2} = \overline{\delta u \delta q^2}$ is normalised by the Kolmogorov velocity scale $u_k = (\nu\epsilon)^{1/4}$ and is plotted as a function of the normalised streamwise separation scale r_1/η. It is of course legitimate to plot $\overline{\delta u \delta q^2}$ as a function of r_1 in principle, but it must be stressed that this plot will be representative of $\overline{\delta u_{||} \delta q^2}$ as a function of r for any direction $\mathbf{r}/r$ only if the small scales are isotropic in the sense defined in the introduction when proceeding from equations 1.6 and 1.7.

The inset in figure 9a shows the same data in a logarithmic scale to stress that the small scales do indeed follow a power law $\propto r^3$ as would be expected by straightforward Taylor expansion if the resolution is adequate. In this inset we also include a straight line representing a power law of exponent 1 for comparison with the r-dependence in equation 1.7.

The most striking observation made when looking at figure 9 is that $\overline{\delta u \delta q^2}$ is positive throughout the range of separations r_1 at x/x_*^{peak}=0.44 and x/x_*^{peak}=0.57 (even though at x/x_*^{peak}=0.57 it is not possible to confirm this within a confidence interval for r/η less

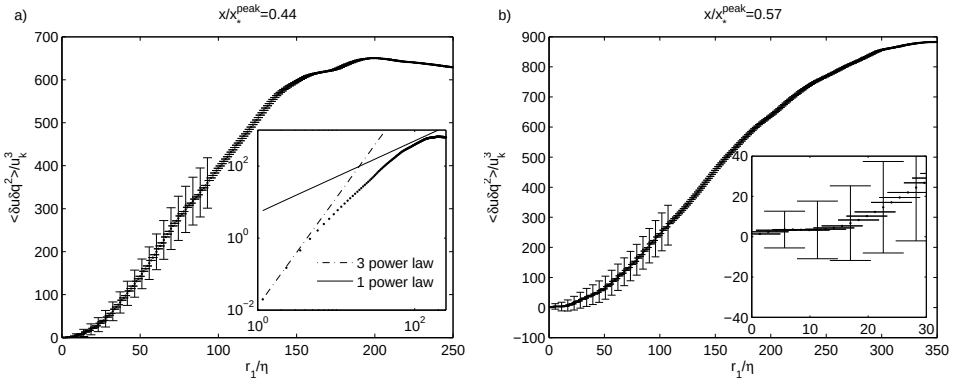

FIGURE 9. Third order structure function $< \delta u \delta q^2 >$ (where $\delta q^2 = \delta u^2 + 2\delta w^2$) normalised by the Kolmogorov velocity u_k versus the streamwise separation r_1 normalised by the Kolmogorov length η at a) x/x_*^{peak}=0.44 and b) x/x_*^{peak}=0.57. Error bars represent a 95% confidence interval for the true value.

than about 40, see the inset of figure 9b). This would imply an inverse energy cascade, i.e. from small to large scales, if the small-scale turbulent fluctuations were isotropic in the sense that equation 1.6 could be used to imply 1.7. As they are not (see section 5), there remains the possibility that the interscale energy transfers are anisotropic allowing for a forward cascade in one direction and an inverse in the other.

It is therefore important to show that $\overline{\delta u \delta q^2}$ is positive within a confidence interval. We choose a 95% confidence interval and use the expression $\pm 1.96\sqrt{\sigma^2_{\delta u \delta q^2}/N}$ where $\sigma^2_{\delta u \delta q^2}$ is the variance of $\delta u \delta q^2$ and N is the number of independent samples. The number of independent samples is chosen on the basis of a bespoke integral length-scale calculated for this purpose by integrating the correlation function of $\delta u \delta q^2(r_1, r_3)$ as in Valente & Vassilicos (2015). The number of independent samples is then estimated by choosing points separated by at least two such bespoke integral length scales resulting in the confidence intervals seen in figure 9. We conclude that $< \delta u \delta q^2 >$ is indeed positive within the chosen 95% confidence interval and that statistical convergence, at least for the sign of $< \delta u \delta q^2 >$, has therefore been achieved.

4. Data reduction

In the present planar PIV experiment the two-point separation vectors are in the PIV xz plane. The separation's streamwise component r_1 is evaluated along the x direction, and the separation's transverse component r_3 along the z direction (see figure 10). In order to obtain the terms in equation 1.2 some assumptions are made because 2D planar PIV does not provide information about the third velocity component (in our case v in the y direction) and about how the second and third order structure functions behave in the y direction. Therefore we assume $\overline{\delta v^2} = \overline{\delta w^2}$, which implies $\overline{\delta q^2}(\mathbf{r}) = \overline{\delta u^2}(\mathbf{r}) + 2\overline{\delta w^2}(\mathbf{r})$, and that the interscale flux vector can be approximated as $\overline{\delta u_i \delta q^2}(\mathbf{r}) \approx \overline{\delta u_i \delta u^2}(\mathbf{r}) + 2\overline{\delta u_i \delta w^2}(\mathbf{r})$.

The various terms in equation 1.2 are estimated by calculating the following statistics where the average is over time: $\overline{\delta u^2}$, $\overline{\delta w^2}$, $\overline{\delta u^3}$, $\overline{\delta w^3}$, $\overline{\delta u \delta w^2}$, $\overline{\delta w \delta u^2}$, $\overline{(w + w')\delta u}$, $\overline{(u + u')\delta u^2}$, $\overline{(w + w')\delta u^2}$, $\overline{(u + u')\delta w^2}$ and $\overline{(w + w')\delta w^2}$ at the two centroids $\mathbf{X} = (0.44x_*^{peak}, 0, 0)$ and $\mathbf{X} = (0.57x_*^{peak}, 0, 0)$ for many different separation vectors (r_1, r_3). Hence, equation

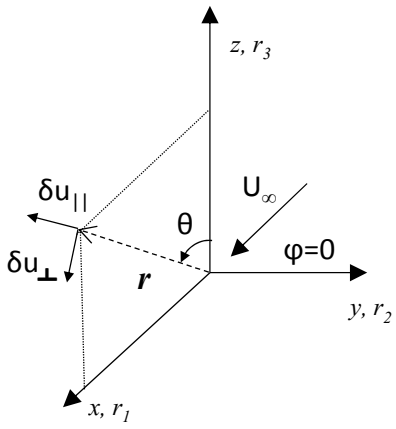

FIGURE 10. Coordinate system. The velocity difference components $\delta u_{||}$ and $\delta u_{\perp}$ lie on the measurement PIV plane. The angle between r_3 axis and $\mathbf{r}$ is denoted θ.

1.2 is evaluated at the two aforementioned centroids both along the centreline of the tunnel. In the z direction, r_3 is limited by the small field of view and attains a maximum value of 26 mm (see figure 5a). In the x direction, r_1 is obtained from Taylor's hypothesis and is sampled to take similar values as our separations r_3.

All statistics are then bi-linearly interpolated into a spherical coordinate system where r_1 is aligned with $(r, \pi/2, 0)$ and r_3 with $(r, 0, 0)$ in the $(r, \theta, \phi = 0)$ plane (see figure 10). The spherical coordinate grid results from the intersections of 19 equally spaced circumferences with 19 equally spaced radial lines between $\theta = 0$ to $\theta = \pi/2$.

Our planar PIV can only access δu and δw. Therefore, we use DNS data of Laizet & Vassilicos (2015) to verify the assumption $\overline{\delta v^2} = \overline{\delta w^2}$. The data we use are from their DNS1-5 which are numerical simulations of turbulence generated by a fractal grid very similar to ours, except that it has $N = 3$ fractal iterations and a thickness ratio $t_r = 8.4$. Figure 11 shows the ratio $\left(\overline{\delta u^2}(\mathbf{r}) + \overline{\delta v^2}(\mathbf{r}) + \overline{\delta w^2}(\mathbf{r})\right) / \left(\overline{\delta u^2}(\mathbf{r}) + 2\overline{\delta w^2}(\mathbf{r})\right)$ for different r_1 and r_3 centred at $x/x^{peak} = 0.44$ (x^{peak} is the actual exact location of the turbulence intensity peak along the centreline). This position corresponds to one of the two ceontroids considered here. We use 960 time steps in total to calculate statistics. Figure 11a shows the results obtained using half of these time steps and figure11b shows the results obtained with all of them. The ratio $\left(\overline{\delta u^2}(\mathbf{r}) + \overline{\delta v^2}(\mathbf{r}) + \overline{\delta w^2}(\mathbf{r})\right) / \left(\overline{\delta u^2}(\mathbf{r}) + 2\overline{\delta w^2}(\mathbf{r})\right)$ varies between 0.85 and 1.15 in figure11b which supports our assumption for the calculation of $\overline{\delta q^2}(\mathbf{r})$. It is also evident from these results that these DNS data are not sufficient to converge higher order statistics and therefore do not allow us to test our second assumption that the interscale flux vector can be approximated as $\overline{\delta u_i \delta q^2}(\mathbf{r}) \approx \overline{\delta u_i \delta u^2}(\mathbf{r}) + 2\overline{\delta u_i \delta w^2}(\mathbf{r})$.

All the terms in equation 1.2 are computed apart form the pressure transport. The derivatives with respect to X_1 and X_3 are computed using a first order forward difference scheme from data at $x/x_*^{peak} = 0.57$ and $x/x_*^{peak} = 0.44$. However, the derivatives with

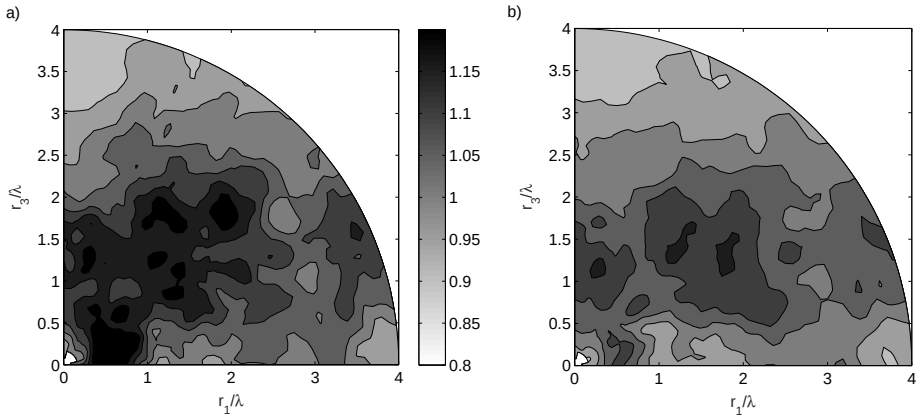

FIGURE 11. Iso-contours of the ratio $\left(\overline{\delta u^2}(\mathbf{r}) + \overline{\delta v^2}(\mathbf{r}) + \overline{\delta w^2}(\mathbf{r})\right) / \left(\overline{\delta u^2}(\mathbf{r}) + 2\overline{\delta w^2}(\mathbf{r})\right)$ using a) 480 time steps and b) 960 time steps. Data of Laizet & Vassilicos (2015).

respect to r_1 and r_3 are computed using a second order central difference scheme (except at the borders where $r_1 = 0$ or $r_3 = 0$ where we use a first order forward difference scheme). Each term is estimated using approximations as in Valente & Vassilicos (2015) which are detailed as follows.

- $\mathcal{A}_t = 0$ because of statistical stationarity and the nature of our averaging operation.

- $4\mathcal{A} \approx (U + U')/2\partial\overline{\delta q^2}/\partial X_1$ because V and W are less than 2% of U and, therefore, considered negligible. The gradient of the mean velocity in the x direction is found to be one order of magnitude smaller than in the z direction (see figure 5b), hence the following approximation is used: $(U + U')/2 \approx (U(X_1, 0, X_3 + r_/3) + U(X_1, 0, X_3 - r_3/2))/2$. We calculate $4\mathcal{A}$ only at $x/x^*_{peak} = 0.44$ because we need the data at $x/x^*_{peak} = 0.57$ to estimate the derivative with respect to X_1. The mean flow data was taken from the large field of view seen in figure 5b.

- $4\Pi \approx 1/r^2\partial/\partial r\left(r^2\overline{\delta u_{||}\delta q^2}\right) + 1/(rsin\theta)\partial/\partial\theta\left(sin\theta\overline{\delta u_\perp \delta q^2}\right)$, where $\delta u_{||}$ and $\delta u_\perp$ are the longitudinal and transverse velocity differences shown in figure 10. The divergence of the energy flux is estimated in spherical coordinates where the contribution from the $\frac{\partial}{\partial\phi}$ term is neglected because we assume the energy flux component in the direction (defined by the unit vector $\hat{r}_\vdash$) normal to the directions marked $\delta u_{||}$ and $\delta u_\perp$ in figure 10 to be approximately independent of the angle ϕ. We cannot test this assumption directly. However we can use the data of Gomes-Fernandes *et al.* (2014) to plot $\overline{(\delta\mathbf{u}.\hat{r}_\vdash)^2}$ at $x/x^{peak}_* = 0.57$ in the r_2r_3 plane and see whether this quantity is approximately independent of ϕ (figure 12). Unfortunately the data of Gomes-Fernandes *et al.* (2014) are insufficient to converge third order statistics such as the relevant component of the energy flux, but figure 12 does provide some indirect support for our assumption albeit on another, yet related, quantity. The wind tunnel experiments of turbulence generated by the same fractal square grid reported by Nagata *et al.* (2013) also support this assumption. These authors found that the one-point kinetic energy and the skewness of the streamwise fluctuating velocity are approximately axisymmetric around the centreline in the production region (and specificially at streamwise distances from the grid very similar to ours in terms of fractions

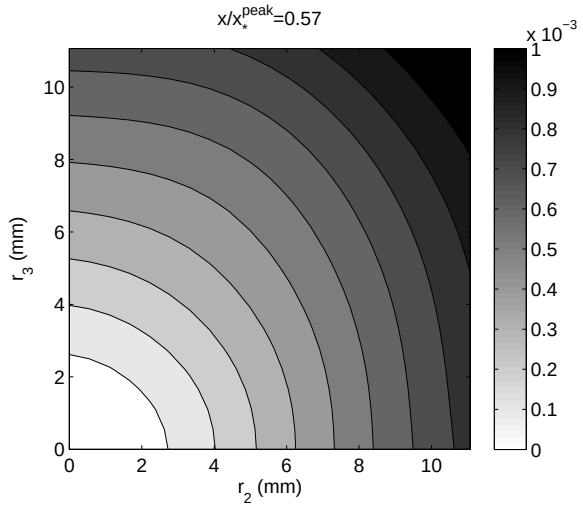

FIGURE 12. Map of $\overline{(\delta\mathbf{u}.\hat{r}_{\vdash})^2}$, in the r_2r_3 plane obtained at $x/x_*^{peak} = 0.57$, where $\hat{r}_{\vdash}$ is a unit vector normal to the directions marked $\delta u_{||}$ and $\delta u_{\perp}$ in figure 10. We used the data presented in Gomes-Fernandes *et al.* (2014) and an additional 2 runs of data at the same location in order to converge the statistics.

of x^*_{peak}) within a radius smaller than 5% of the tunnel width. The maximum separation r ($\approx 26mm$) considered in the present statistics is always smaller than 5% of our channel width, and it is reasonable to assume that the two-point statistics involved in the definition of 4Π should also be axisymmetric under such conditions. We calculate 4Π at both $x/x^*_{peak} = 0.44$ and 0.57 where the field of view is wide enough in the r_3 direction.

• $4\Pi_U \approx \partial\delta U\overline{\delta q^2}/\partial r_1$ where we effectively assume $V = W = 0$ as we are on the centreline or very near it. Due to centreline symmetry, $U(X_1, 0, r_3/2) \approx U(X_1, 0, -r_3/2)$ and δU is only non-zero for $r_3 \neq 0$. Since U is a slowly varying function of x (or X_1) we approximate δU with a Taylor expansion $\delta U \approx r_1\partial U/\partial x$ and we use a second order central difference scheme to estimate it at $x/x^*_{peak} = 0.44$ with data from $x/x_*^{peak} = 0.20$ and 0.57;

• $4\mathcal{P} \approx 2\overline{\delta u^2}\partial U/\partial x + 2\overline{(w + w')\delta u}\partial U/\partial z$ as V and W are again assumed equal to zero as well as $\partial U/\partial y$ and $\partial U'/\partial y'$ because of the mean flow symmetry in the xz plane. In addition, symmetry of the flow in relation to the centreline is invoked as $\partial U/\partial z \approx -\partial U'/\partial z'$ as well as the approximation that $\partial U/\partial x \approx \partial U'/\partial x'$. The gradient $\partial U/\partial z$ is taken from a second degree polynomial function fitted to the data in figure 5b at $x/\eta = 0$;

• $4\mathcal{T} \approx -\partial/\partial X_1(\overline{(u + u')\delta q^2}/2) - \partial/\partial X_3(\overline{(w + w')\delta q^2})$ where the derivative in X_3, $\partial/\partial X_3(\overline{(w + w')\delta q^2}/2)$, is assumed equal to $\partial/\partial X_2(\overline{(v + v')\delta q^2}/2)$ given the 90^o statistical flow symmetry about the centreline. The transverse derivative is estimated by taking another centroid along the z axis where $z = 13mm$ (see figure 5a). The results were checked and were found not to be significantly sensitive to the z coordinate chosen around this value. The term $4\mathcal{T}$ was estimated at $x/x^*_{peak} = 0.44$ using data from $x/x_*^{peak} = 0.57$.

- The pressure transport $4\mathcal{T}_p$ cannot be estimated with the present data.

- $4\mathcal{D}_\nu \approx 2\nu/r^2\partial/\partial r(r^2\partial\overline{\delta q^2}/\partial r)$ plus polar and azimuthal contributions which cancel out when averaged over spherical shells. Here we only calculate the radial contribution to $4\mathcal{D}_\nu$ at $x/x^*_{peak} = 0.44$ and 0.57. Note that $4\mathcal{D}_\nu$ tends to $\epsilon(\mathbf{X})$ when the scale separation tends to zero. It was also mathematically shown in Laizet *et al.* (2013) and Valente & Vassilicos (2015) that $4\mathcal{D}_\nu$ is small compared to $\epsilon(\mathbf{X})$ when r is larger than the Taylor microscale.

- $4\mathcal{D}_{X,\nu} \approx \nu/2\partial^2/\partial X_1^2(\overline{\delta q^2}) + \nu\partial^2/\partial X_3^2(\overline{\delta q^2})$ where use is again made of 90^o symmetry about the centreline. The streamwise second order derivative is only computed for $r_3 = 0$ using data from stations $x/x_*^{peak} = 0.20$, 0.44 and 0.57. Hence we estimate $4\mathcal{D}_{X,\nu}$ only at $x/x_*^{peak} = 0.44$. Valente & Vassilicos (2015) reported that this term is negligibly small for the decay region of regular grids and we confirm that the same holds in the production region of our fractal grid by calculating this term for several r_1 separations (see section 6). The second order derivative in the z direction (assumed equal to the one in y direction, given the 90^o symmetry) is estimated using the statistical symmetry with respect to the centreline in the zx plane where it becomes $2(\overline{\delta q^2}(X_1, 0, \Delta z; \mathbf{r}) - \overline{\delta q^2}(X_1, 0, 0; \mathbf{r}))/\Delta z^2$ ($\Delta z = 13mm$);

- $4\epsilon^* = 4(\epsilon + \epsilon')/2$ where we use the surrogate $3\nu(\overline{s_{11}^2} + \overline{s_{22}^2}) + 12\nu\overline{s_{12}^2}$ with $s_{ij} = 1/2(\partial u_i/\partial x_j + \partial u_j/\partial x_i)$ (Tanaka & Eaton 2007) to estimate the energy dissipation at **x** and **x'**. To estimate ϵ and ϵ' from the small field of view which does not allow r_1 values beyond the resolution scale, we use the observation that ϵ and ϵ' are about equal along a $z = const$ line. This observation is supported by figure 13 where we plot a xz map of ϵ calculated from the large field of view at $x/x^*_{peak} = 0.44$. This figure shows clearly that ϵ varies significantly along z but very little along x. Even though the spatial resolution in this figure is relatively low (close to 8.4η on the centreline, see table 3), we do not expect the qualitative behaviour to change much with increased resolution.

- $4\mathcal{B} = 4\mathcal{A} + 4\Pi + 4\Pi_U - 4\mathcal{P} - 4\mathcal{T} - 4\mathcal{D}_\nu - 4\mathcal{D}_{X,\nu} + 4\epsilon^*$ where each one of these terms is calculated as described in the preceding bullet points. $4\mathcal{B}$ is therefore the remainder required to satisfy the Kármán-Howarth balance 1.2. This remainder may be expected to be dominated by the pressure transport $4\mathcal{T}_p$ which we are unable to measure, but it can also have contributions coming from the simplifying assumptions we made when estimating all the other terms.

5. Non-linear energy transfer between scales

Having obtained positive values for $\overline{\delta u \delta q^2}$ (figure 9) we now plot iso-contours of $\overline{\delta u_{||} \delta q^2}$ which show how this quantity depends on r_1 and r_3 at $x/x_*^{peak} = 0.44$ and 0.57. This map (figure 14) shows that $\overline{\delta u_{||} \delta q^2}$ is not isotropic at the scales considered and is therefore different from $\overline{\delta u \delta q^2}$. Hence, equation 1.7 does not follow from equation 1.6 at the locations where we measure in this turbulent flow and must not be expected to hold. In fact, figure 14 shows that $\overline{\delta u_{||} \delta q^2}$ has different signs at different values of (r_1, r_3) which invalidates equation 1.7 at a stroke.

Figure 15 shows the iso-contours of the second order structure function $\overline{\delta q^2}(r_1, r_3)$ at $x/x_*^{peak} = 0.44$ and 0.57. It may be interesting to note that $\overline{\delta q^2}(r_1, r_3)$ is much more isotropic than $\overline{\delta u_{||} \delta q^2}$. In fact, in terms of spherical coordinates (see figure 10), the

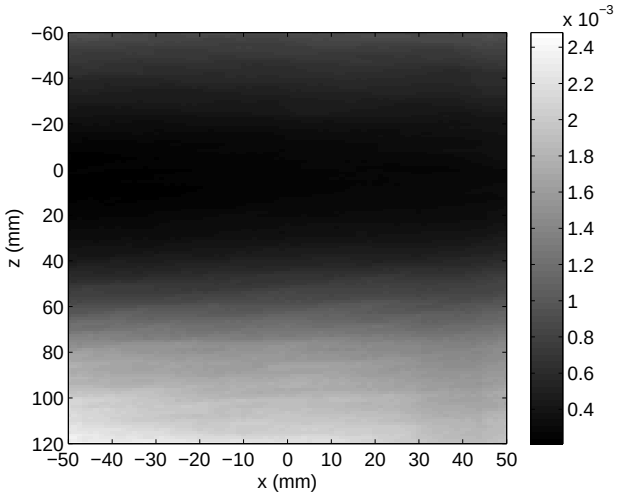

FIGURE 13. Turbulent energy dissipation ϵ $(m^4 s^{-3})$ map in the xz plane at $x/x_*^{peak} = 0.44$.

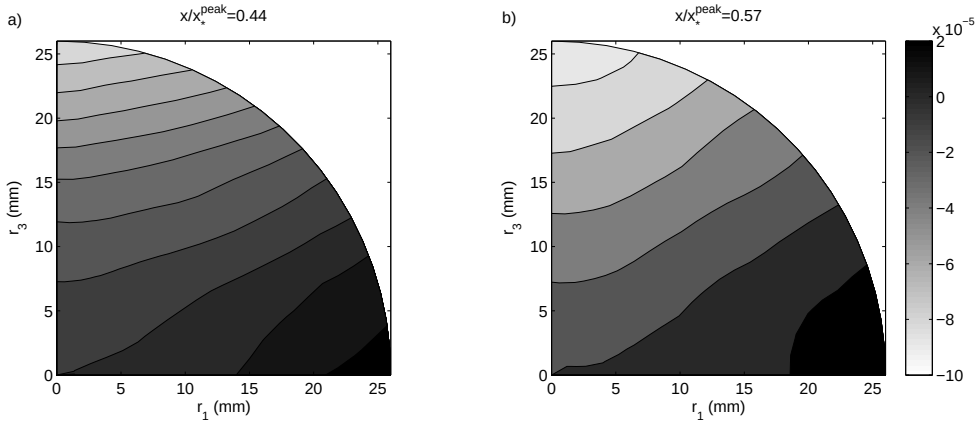

FIGURE 14. Iso-contours of the parallel third order structure function $\overline{\delta u_{||} \delta q^2}$ $(m^3 s^{-3})$ at a) $x/x_*^{peak} = 0.44$ and b) $x/x_*^{peak} = 0.57$.

variation of $\overline{\delta q^2}(r, \theta, \phi = 0)$ with angle θ shows that $\overline{\delta q^2}$ becomes more isotropic from $x/x_*^{peak} = 0.44$ to 0.57 as the iso-contours become more circular. Note also that in the production region where the present measurements are taken, turbulence intensity increases along the streamwise direction and so does the energy contained within a specific separation vector (r_1, r_3) in figure 15.

The possibility of a forward cascade in one direction and an inverse cascade in the other has already been mentioned in section 3.2 and the different signs of $\overline{\delta u_{||} \delta q^2}$ for different separation vectors (r_1, r_3) in figure 14 support such a view. Following Lamriben *et al.* (2011) and Valente & Vassilicos (2015), we plot the fluxes $\overline{\delta u_i \delta q^2}$ in figures 16a and 17a for $x/x_*^{peak} = 0.44$ and 0.57 respectively. The directions of these flux vectors show an inverse cascade roughly aligned with an axis at a small angle from the streamwise (r_1 and velocity component u) direction, and a forward cascade roughly aligned in the lateral (r_3 and velocity component w) direction for r_1 is small. For separation vectors

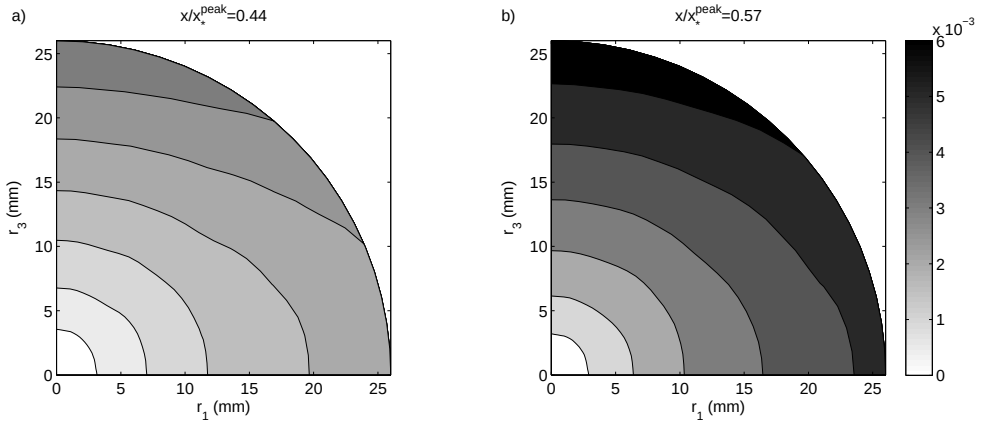

FIGURE 15. Iso-contours of the second order structure function $\overline{\delta q^2}$ ($m^2 s^{-2}$) at a) $x/x_*^{peak} = 0.44$ and b) $x/x_*^{peak} = 0.57$.

between these two extremes, the interscale energy flux is in an intermediate state where the cascade is both forward and inverse in different components of the flux vector, i.e. forward in the longitudinal and inverse in the streamwise projections of this vector. For separation vectors between the streamwise direction and the aforementioned axis at a slight angle to this direction, the cascade is purely inverse.

Writing the non-linear energy transfer term $4\Pi(\mathbf{X}, \mathbf{r}) = \partial\overline{\delta u_i \delta q^2}/\partial r_i$ in spherical coordinates as in section 4 and integrating over the solid angle one immediately gets

$$\int 4\Pi \, d\Omega = \int 4\Pi_r \, d\Omega \tag{5.1}$$

where $\Pi_r = 1/r^2 \partial/\partial r \left(r^2 \overline{\delta u_{||} \delta q^2} \right)$ is the radial part of the divergence of $\overline{\delta u_i \delta q^2}$. This relation between two integrals simply states that when averaged over all directions, the non-linear interscale energy transfers are fully determined only by the radial part Π_r of the interscale flux divergence. We therefore plot Π_r in figures 16b and 17b but remain mindful of the limitations imposed by our measurement capabilities which mean that we can only plot iso-contours of Π_r in the $\phi = 0$ plane (see figure 10). The white contour indicates the transition between negative and positive values for Π_r in agreement with the behaviour of the flux vectors. This is another way to extract from the data the information that the cascade in the two production region locations considered here is both forward and inverse, the inverse part operating mostly in the streamwise direction whereas the forward part operates mostly in the lateral direction along z.

It may be worth pointing out that the energy spectra at the centreline positions $x/x_*^{peak} = 0.44$ and $x/x_*^{peak} = 0.57$ where we find this combination of forward and inverse cascades have power law spectra with exponents close to $-5/3$ (see figure 8a,b). In fact the inverse part of the cascade is around the streamwise direction. This is also the direction for which these $E_{11}(k_1)$ energy spectra are calculated, the wavenumber k_1 corresponding to the frequency f in figure 8 by Taylor's hypothesis $k_1 = fU_1$ (see appendix A for our validation of the Taylor hypothesis in the present context).

To evaluate whether the cascade is overall forward or inverse at a given separation $|\mathbf{r}| = r$, we need to integrate Π over the angles θ and ϕ (see figure 10). However, our data do not allow us to calculate the integrals in equation 5.1 because they are confined to the

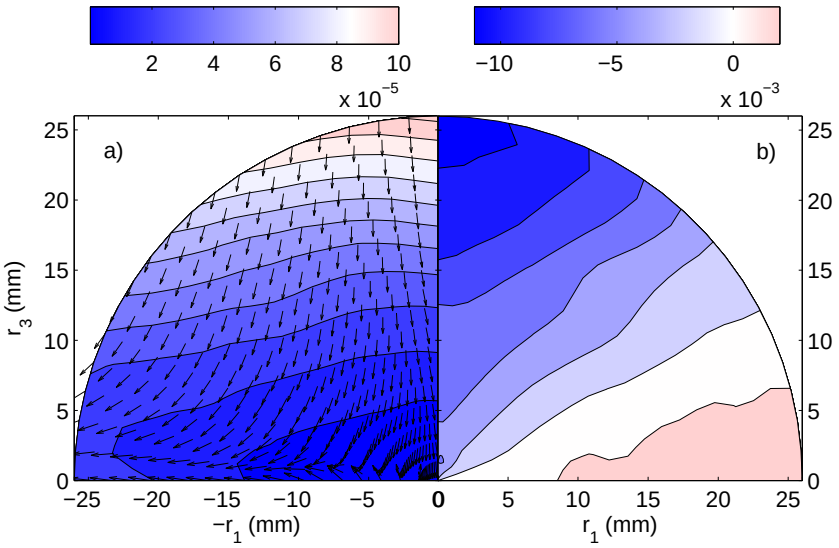

FIGURE 16. a) Third order structure function vectors $\overline{\delta u_i \delta q^2}$ and iso-contours of their magnitude and b) iso-contours of the radial part of the divergence of $\overline{\delta u_i \delta q^2}$ at $x/x_*^{peak} = 0.44$.

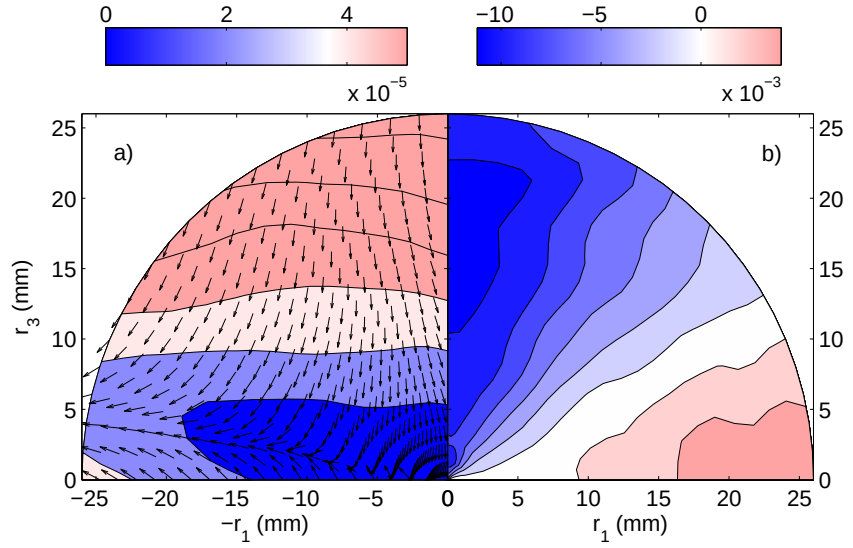

FIGURE 17. a) Third order structure function vectors $\overline{\delta u_i \delta q^2}$ and iso-contours of their magnitude and b) iso-contours of the radial part of the divergence of $\overline{\delta u_i \delta q^2}$ at $x/x_*^{peak} = 0.57$.

plane $\phi = 0$. Nevertheless, we can calculate $\int_0^{\pi/2} \Pi d\theta$ and $\int_0^{\pi/2} \Pi_r d\theta$ using the reduced form for Π in section 4. We find these two integrals to be very close to each other at both centreline positions $x/x_*^{peak} = 0.44$ and $x/x_*^{peak} = 0.57$. In fact, Laizet & Vassilicos (2011) and Nagata *et al.* (2013) have shown that in a transverse planar region around the centreline of size less than about $L_0/10$ at these positions ($L_0/10$ corresponds to

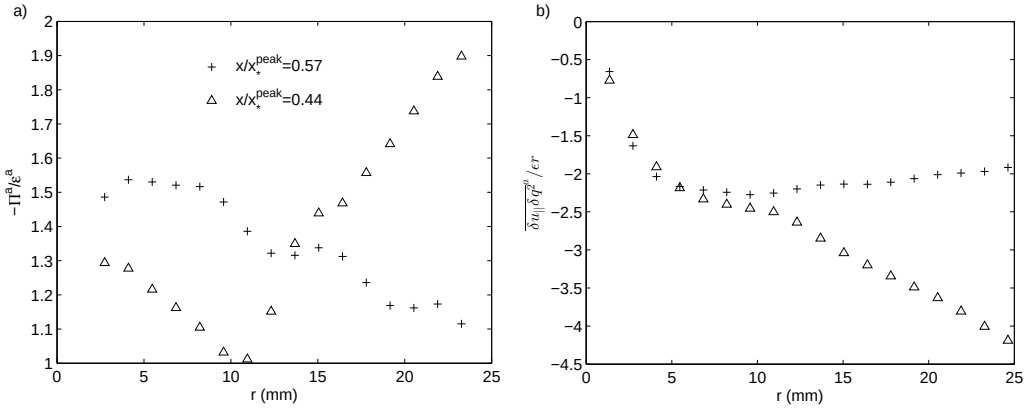

FIGURE 18. a) Circumferentially averaged non-linear energy transfer term Π^a normalised by the similarly averaged energy dissipation ϵ^a. b) Circumferentially averaged parallel third order structure function compensated by $\epsilon^a r$, i.e. $\overline{\delta u_{||} \delta q^2}^a / \epsilon r$ as a function of r (mm) at $x/x_*^{peak} = 0.44$ and $x/x_*^{peak} = 0.57$.

about 30mm here) the one-point turbulence statistics are approximately axisymmetric around the streamwise axis, i.e. independent of ϕ. Their result is consistent with our finding that $\int_0^{\pi/2} \Pi d\theta \approx \int_0^{\pi/2} \Pi_r d\theta$ which is implied from equation 5.1 when Π and Π_r are independent of the angle ϕ.

In figure 18a we plot $-\Pi^a \equiv -\frac{2}{\pi}\int_0^{\pi/2} \Pi d\theta$ normalised by $\epsilon^a \equiv \frac{2}{\pi}\int_0^{\pi/2} \epsilon^* d\theta$ as a function of $r = |\mathbf{r}|$. The first observation is that, regardless of the inverse and forward cascade mix evident in the previous statistics, the sign of Π^a is negative for all separations r considered here. This indicates an overall forward cascade when integrated over the different directions. The second observation is that $-\Pi^a/\epsilon^a$ takes values between 1 and 2 at $x/x_*^{peak} = 0.44$ and between 1.1 and 1.6 at $x/x_*^{peak} = 0.57$ where the -5/3 spectrum is particularly well defined (see figure 8). Note that when we normalise $-\Pi^a$ by ϵ (i.e. ϵ^* at $\mathbf{r} = \mathbf{0}$), the plots in figure 18a do not change much and in fact, for the case where $x/x_*^{peak} = 0.57$, $-\Pi^a/\epsilon$ varies between 1.2 and 1.5. There is therefore some tendency for $-\Pi^a$ to be close to a constant at $x/x_*^{peak} = 0.57$ though far from perfectly so. This suggests a cascade which is approximately self-similar in scales when directions have been integrated out.

A functional form for the directionally averaged interscale flux $\overline{\delta u_{||} \delta q^2}^a = \frac{2}{\pi}\int_0^{\pi/2} \overline{\delta u_{||} \delta q^2} d\theta$ can be derived from the observation that $-\Pi^a$ is not too far from a constant and using $r^2 4\Pi^a = \frac{2}{\pi}\int_0^{\pi/2} \frac{\partial}{\partial r}(r^2 \overline{\delta u_{||} \delta q^2}) d\theta = \frac{\partial}{\partial r}(r^2 \overline{\delta u_{||} \delta q^2}^a)$. Integrating with respect to r (starting from $r = 0$) while assuming that Π^a is constant yields

$$\overline{\delta u_{||} \delta q^2}^a = 4\Pi^a r/3 \, . \tag{5.2}$$

In figure 18b we plot $\overline{\delta u_{||} \delta q^2}^a/(\epsilon r)$ versus r and see that, at $x/x_*^{peak} = 0.57$ where the -5/3 is most clearly present (figure 8), $\overline{\delta u_{||} \delta q^2}^a \approx -16\epsilon r/9$ (consistent with equation 5.2 and $\Pi^a \approx -4\epsilon/3$ from figure 18a) but with a small drift away from this expression. Hence, even though equation 1.7 does not hold here, a relation similar to it does hold at $x/x_*^{peak} = 0.57$ when averaging over separation vector orientations. (Note also that figure 18b remains roughly the same when plotting $\overline{\delta u_{||} \delta q^2}^a/(\epsilon^a r)$ rather than $\overline{\delta u_{||} \delta q^2}^a/(\epsilon r)$.)

We now make a final set of observations which relate to equation 1.5 in the introduction. This equation is central to the Richardson-Kolmogorov cascade and is typically derived by assuming local homogeneity and local equilibrium 1.5. It implies, in particular, that the non-linear energy transfer term (or divergence of the interscale energy flux) Π is independent of the orientation of the separation vector $\mathbf{r}$. We have seen that the radial part Π_r of the divergence of the interscale energy flux is not independent of orientation (figures 16 and 17) but as shown in figure 19, Π does nevertheless turn out to be fairly isotropic at $x/x_*^{peak} = 0.57$ though not at $x/x_*^{peak} = 0.44$. Note also that the values of Π are negative at both locations $x/x_*^{peak} = 0.44$ and 0.57 for all separations probed here and that they do not vary much with $\mathbf{r}$ at $x/x_*^{peak} = 0.57$. We are therefore presented with a situation at $x/x_*^{peak} = 0.57$ where Π is negative and approximately uniform in value across our separation vectors, a situation very similar to equation 1.5. Yet, as mentioned in the first paragraph of this section, equation 1.7 does not hold at our measurement stations.

The violation of 1.7 results from the combined forward and inverse cascades already mentioned. The negative values of Π throughout our $\mathbf{r}$ plane result from non-linear energy transfers from one orientation of $\mathbf{r}$ to another at constant $r = |\mathbf{r}|$. It has to do with the topology of the interscale flux vector field in $\mathbf{r}$ space (see figures 16a and 17a). The seemingly attracting inverse cascade axis which lies at a small angle to the streamwise direction (see figures 16a and 17a) imposes a negative transfer in orientations (from $\theta = \pi/2$ to smaller) between this axis and the streamwise direction (where $\Pi_r > 0$) and a positive transfer in orientations (towards increasing angles θ) in the rest of the $\mathbf{r}$ plane (where $\Pi_r < 0$). As the circumferentially averaged transfer in orientations equals 0, i.e. as $\int_0^{\pi/2} \Pi d\theta = \int_0^{\pi/2} \Pi_r d\theta$, and as the negative transfer in orientations (from $\theta = \pi/2$ to 0) is confined over a region in the $\mathbf{r}$ plane which is significantly smaller than the region where the transfer in orientations is positive (i.e. towards increasing angles θ), we can expect the negative values of $\Pi - \Pi_r$ (confined to the region where $\Pi_r > 0$) to be significantly larger in magnitude than the positive values of $\Pi - \Pi_r$ (in the rest of the $\mathbf{r}$ plane where $\Pi_r < 0$). These kinematic considerations explain why Π can be negative throughout $\mathbf{r}$ as indeed observed, but do not explain why it actually is negative at both $x/x_*^{peak} = 0.44$ and 0.57 and approximately uniform in $\mathbf{r}$ at $x/x_*^{peak} = 0.57$.

We close this section with a summary of our findings so far.

(i) At our measurement stations in the production region around centreline points $x/x_*^{peak} = 0.44$ (where $Re_\lambda = 190$) and $x/x_*^{peak} = 0.57$ (where $Re_\lambda \approx 270$) the interscale energy transfers are characterised by a combination of an inverse cascade along an attracting axis at a small angle to the streamwise direction and a forward cascade in the transverse direction. For this reason there is no relation such as equation 1.7 valid at these production region points and there is no small-scale isotropy either.

(ii) Nevertheless, there is a well-defined -5/3 streamwise energy spectrum $E_{11}(k_1)$, particularly at $x/x_*^{peak} = 0.57$ where $Re_\lambda \approx 270$.

(iii) The directionally averaged cascade is forward, i.e. from large to small scales, and the r-dependence of $\overline{\delta u_{||} \delta q^2}^a$ is not too far from $\overline{\delta u_{||} \delta q^2}^a = -16\epsilon r/9$ at $x/x_*^{peak} = 0.57$. The coefficient 16/9 should not be given too much significance as it can be expected to be, at least residually, Reynolds number dependent.

(iv) Even without directional averages, Π is negative at both $x/x_*^{peak} = 0.44$ and 0.57 and approximately uniform in $\mathbf{r}$ at $x/x_*^{peak} = 0.57$. This results from the combination of nonlinear transfers across separation scales and across separation orientations.

In the following section we show that the turbulence at these measurement stations

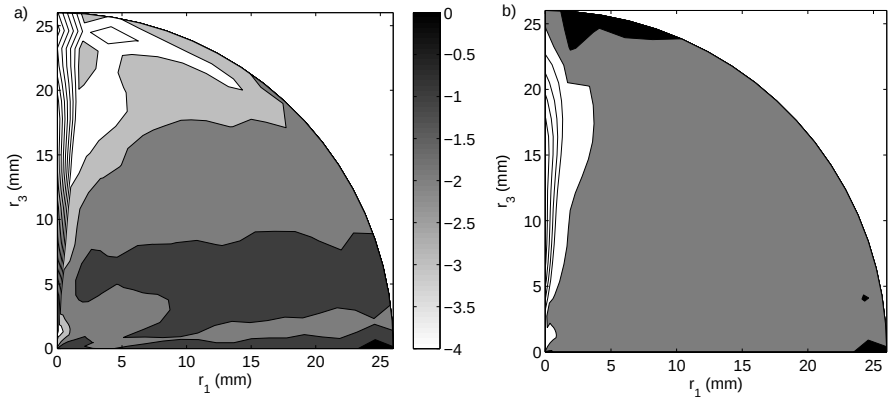

FIGURE 19. Non-linear energy transfer term normalised by energy dissipation, Π/ϵ^*, at a) $x/x_*^{peak} = 0.44$ and b) $x/x_*^{peak} = 0.57$.

is not homogeneous at the scales r considered and that it is therefore not possible to reduce the inhomogeneous Kármán-Howarth equation 1.2 to the simpler form 1.3 which is typically used to derive the Richardson-Kolmogorov cascade and its consequences from Kolmogorov's assumption of local equilibrium.

6. Energy transfer budget

6.1. *Small and negligible terms*

The energy transfer via the mean velocity gradients Π_U, the viscous transport $\mathcal{D}^*_{X,\nu}$ and the viscous diffusion $\mathcal{D}^*_\nu$ are found to be small compared to the other terms in equation 1.2 that we can estimate and in particular small compared to ϵ^*.

Figure 20a shows the flux vector $(\delta U\overline{\delta q^2}, 0, 0)$ $(m^3 s^{-3})$ (see data reduction in section 4) and the iso-contours of its magnitude $|\delta U\overline{\delta q^2}|$ whereas figure 20b presents the divergence of this flux, Π_U, which is normalised by ϵ^*. The divergence of $\delta U\overline{\delta q^2}$ takes maximum values at separations that have large r_1 and small r_3 values. These maximum values are of the order of $0.25\epsilon^*$. For similar separations (r_1,r_3), advection $\mathcal{A}$ takes on values close to $9\epsilon^*$ (see figure 22a) and turbulent transport $\mathcal{T}$ close to $10\epsilon^*$ (see figure 22b) which makes the divergence of $\delta U\overline{\delta q^2}$ negligible. In fact, as a cursory comparison of figures 20b and 22 rightly suggest, Π_U is much smaller than both $\mathcal{A}$ and $\mathcal{T}$ at all $\mathbf{r}$.

The viscous diffusion term, $\mathcal{D}_{X,\nu}$ was estimated for $r_3 = 0$ and was found to be two orders of magnitude smaller than ϵ^* irrespective of r_1. It is therefore, as expected, not considered important for the Kármán-Howarth two-point energy budget.

Figure 21 is a plot of the r-dependencies of $\Pi^a_U = \frac{2}{\pi}\int_0^{\pi/2} \Pi_U d\theta$ and $\mathcal{D}^a_\nu = \frac{2}{\pi}\int_0^{\pi/2} \mathcal{D}_\nu d\theta$ normalised by $\epsilon^a = \frac{2}{\pi}\int_0^{\pi/2} \epsilon^* d\theta$. This figure shows that viscous diffusion tends to increase with decreasing r which agrees with the constraint that $\mathcal{D}_\nu$ tends to $\epsilon(\mathbf{X})$ as r tends to 0. The maximum values of $\Pi^a_U + \mathcal{D}^a_\nu$ are below about 30% of the energy dissipation which is negligible when compared with the other terms estimated in section 6.2.

6.2. *Main terms*

Figure 22 is a plot in (r_1, r_3) space of the advection $(\mathcal{A})$ and turbulent transport $(\mathcal{T})$ terms normalised by energy dissipation ϵ^*. Both terms are shown to be fairly isotropic

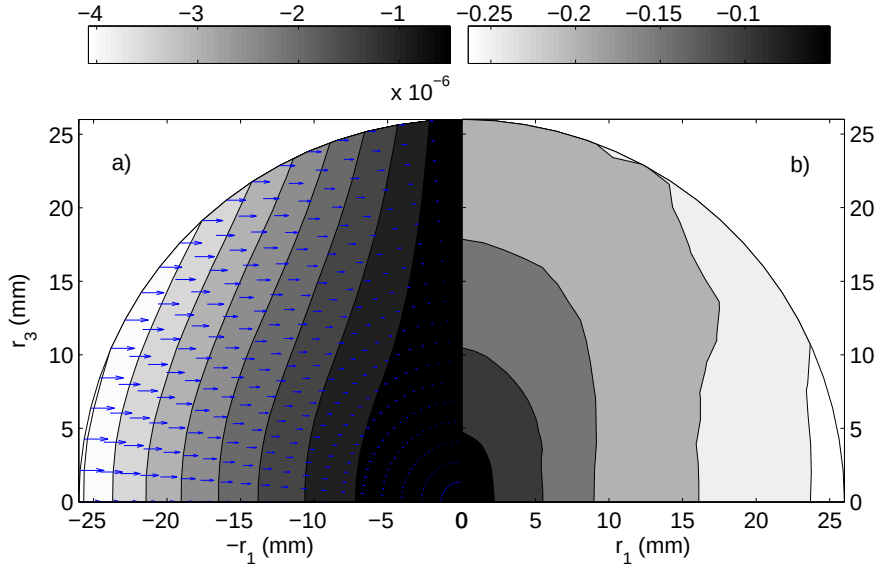

FIGURE 20. a) Linear flux field $(\delta U, 0)\overline{\delta q^2}$ $(m^3 s^{-3})$ together with the iso-contours of its magnitude $|\delta U \overline{\delta q^2}|$ $(m^2 s^{-2})$. b) Iso-contours of Π_U/ϵ^* at $x/x_*^{peak} = 0.44$.

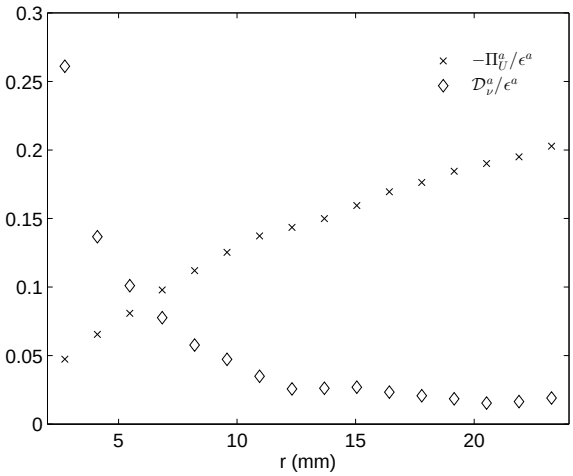

FIGURE 21. Circumferentially averaged energy transfer by the mean velocity gradients Π_U^a and viscous diffusion $\mathcal{D}_\nu^a$ normalised by the circumferentially averaged energy dissipation ϵ^a at $x/x_*^{peak} = 0.44$.

in the sense that their contour lines resemble circles, at least up to the maximum radius considered here. In addition, given that their magnitudes are roughly similar particularly at the smaller scales, there seems to be a tendency for these two terms to cancel much (though not all) of each other in equation 1.2.

Figure 23 is also a plot in (r_1, r_3) space but of the production $(\mathcal{P})$ and of the remainder $-\mathcal{B}$ of the Kármán-Howarth-Monin balance 1.2 both normalised by ϵ^*. Both these terms are larger than energy dissipation for transverse separations r_3 that are not too small.

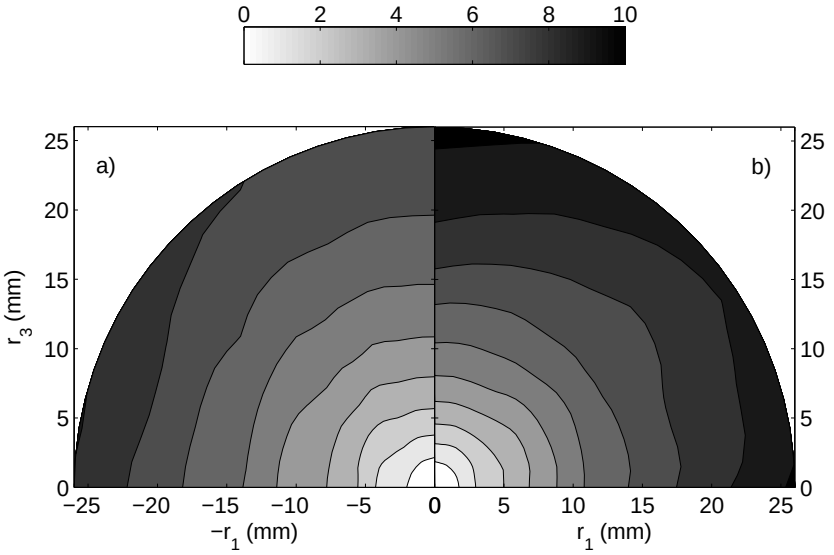

FIGURE 22. a) Advection term normalised by energy dissipation, $\mathcal{A}/\epsilon^*$ and b) turbulence transport normalised by energy dissipation, $\mathcal{T}/\epsilon^*$ at $x/x_*^{peak} = 0.44$.

This is not surprising for the production term as, in the production region, turbulence intensity and $\overline{\delta q^2}$ (see figure 15) increase with streamwise distance from the grid. Qualitatively, these terms behave differently compared to advection and turbulent transport in figure 22. The main difference is that the contours appear stratified in figure 23 as opposed to circular in figure 22. The stratification of the production term in the r_3 direction (figure 23a) is due to the mean velocity gradients being much larger in that direction than in the r_1 direction. This fact is patent in the mean velocity field, see figure 5b.

Besides Π and ϵ^*, the main terms in the Kármán-Howarth-Monin balance 1.2 at the location of the production region where we can estimate them ($x/x_*^{peak} = 0.44$) are $\mathcal{A}$, $\mathcal{T}$, $\mathcal{P}$ and $-\mathcal{B}$. The approximate Kármán-Howarth-Monin balance that we are therefore faced with is

$$\Pi \approx -\epsilon^* + \mathcal{P} + (\mathcal{T} - \mathcal{A}) + \mathcal{B} \tag{6.1}$$

where we might expect a significant part of $\mathcal{B}$ to be the pressure transport term $\mathcal{T}_p$, see section 4. Laizet & Vassilicos (2012) reported that at a distance $x/x_*^{peak} = 0.44$ from a turbulence-generating fractal grid similar to ours, the average pressure is still recovering.It is indeed reasonable to expect the pressure transport term $\mathcal{T}_p$ to be important in the production region.

In figure 24 we plot the terms in equation 6.1 at $x/x_*^{peak} = 0.44$ but averaged over θ and normalised by $\epsilon^a = \frac{2}{\pi}\int_0^{\pi/2} \epsilon^* d\theta$. The production term $\mathcal{P}^a = \frac{2}{\pi}\int_0^{\pi/2} \mathcal{P} d\theta$ is positive, meaning production of turbulence fluctuations by the mean flow, and is comparable to the non-linear energy transfer $-\Pi^a = -\frac{2}{\pi}\int_0^{\pi/2} \Pi d\theta$. The terms of highest magnitude, however, are the advection $\mathcal{A}^a = \frac{2}{\pi}\int_0^{\pi/2} \mathcal{A} d\theta$ and the turbulent transport $\mathcal{T}^a = \frac{2}{\pi}\int_0^{\pi/2} \mathcal{T} d\theta$, both positive, and the remainder $\mathcal{B}^a = \frac{2}{\pi}\int_0^{\pi/2} \mathcal{B} d\theta$ which turns out negative. As already mentioned, Π^a is negative but also, perhaps remarkably, varies less with r than all the

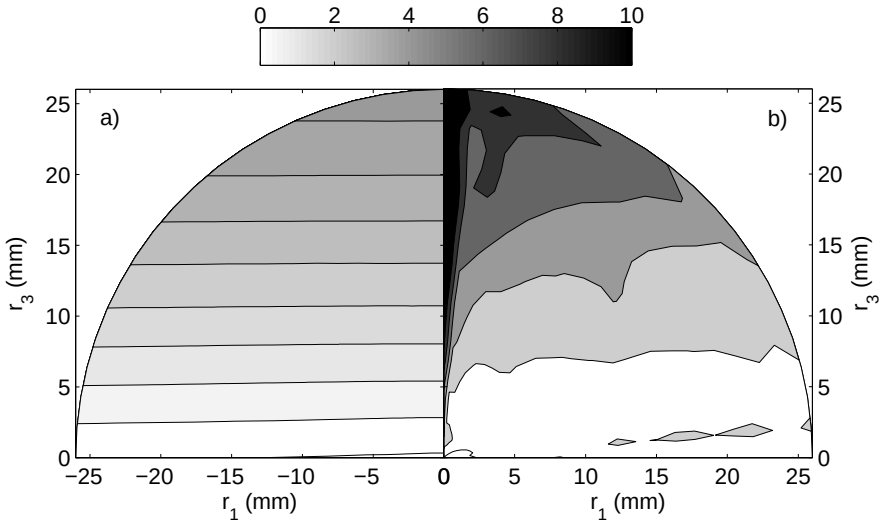

FIGURE 23. a) Production term normalised by energy dissipation, $\mathcal{P}/\epsilon^*$ and b) the remainder of the Kármán-Howarth balance normalised by energy dissipation, $-\mathcal{B}/\epsilon^*$ at $x/x_*^{peak} = 0.44$.

other terms in equation 6.1. Combining expression 6.1 with 5.2 which follows from the near-constancy of Π^a, we obtain

$$\overline{\delta u_{||} \delta q^2}^a \approx -\frac{4}{3} r \left(\epsilon^a - \mathcal{P}^a - (\mathcal{T}^a - \mathcal{A}^a) - \mathcal{B}^a\right) \tag{6.2}$$

which is similar to 1.7, in particular because $\epsilon^a - \mathcal{P}^a - (\mathcal{T}^a - \mathcal{A}^a) - \mathcal{B}^a$ (which turns out to be approximately equal to $4/3\epsilon^a$ here, see paragraph under equation 5.2) is only weakly dependent on r, yet very different.

7. Conclusions

The focus of this work has been in the two-point statistics of turbulence fluctuations in the most inhomogeneous and anisotropic region of grid-generated turbulence. This region is termed the production region and lies between the grid and the peak of turbulence intensity downstream of it. In order to magnify the space where PIV can be performed and to capture the smallest scales of the flow while maintaining a good dynamic range in space, we have used a well-documented turbulence-generating fractal square grid which is known to magnify the streamwise extent of the production region and abate its turbulence activity. We performed planar two-component PIV measurements of many terms of the non-homogeneous Kármán-Howarth-Monin equation in this region. We found the turbulence to be indeed significantly inhomogeneous and anisotropic even at scales smaller than the Taylor microscale around the centre of that region on the centreline. The two-point advection and transport terms are dominant and the production is significant too in the Kármán-Howarth-Monin balance. The importance of the two-point advection indicates that one cannot apply the local equilibrium hypothesis 1.4 of Kolmogorov. It is therefore impossible to apply usual Kolmogorov arguments based on the Kármán-Howarth-Monin

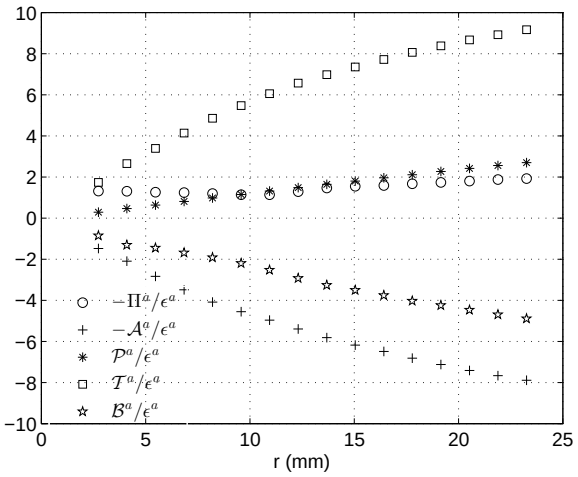

FIGURE 24. Circumferentially averaged non-linear energy transfer ($-\Pi^a$), advection ($-\mathcal{A}^a$), production ($\mathcal{P}^a$), turbulent transport ($\mathcal{T}^a$) and remainder $\mathcal{B}^a$ normalised by circumferentially averaged energy dissipation ϵ^a at $x/x_*^{peak} = 0.44$.

equation and resulting dimensional considerations to deduce interscale flux and spectral properties.

We find that the interscale energy transfers are characterised by a combination of an inverse cascade along an attractive axis, which is at a small angle with the streamwise direction and a forward cascade in the transverse direction. For this reason there is no relation such as equation 1.7, which requires a forward cascade for all separations, valid at our production region points and there is no small-scale isotropy either. Even so, the energy spectrum of the streamwise fluctuating component exhibits a well-defined -5/3 power law over one decade.

The directionally averaged cascade is forward, i.e. from large to small scales, and the r-dependence of $\overline{\delta u_{||} \delta q^2}^a$ is not too far from linear in r at $x/x_*^{peak} = 0.57$. *The directionally averaged non-linear energy transfer term* Π^a *is negative and varies less with* r *than all the other terms in the approximate Kármán-Howarth-Monin balance 6.1.*

Even without directional averages, Π is negative at both $x/x_*^{peak} = 0.44$ and 0.57 and approximately uniform in $\mathbf{r}$ at $x/x_*^{peak} = 0.57$. This results from the combination of nonlinear transfers across separation orientations as well as across scales.

Note that power-law energy spectra with exponents close to -5/3 have also been reported in a cylinder wake within one cylinder diameter from the cylinder (Braza *et al.* 2006). It might be relevant to perform studies similar to ours in various very near-field wakes and determine their intercale nonlinear cascade characteristics. In future works on near-field wakes and on the production region of grid-generated turbulence it will also be important to examine the assumptions that we were forced to make as a result of the 2D planar nature of our PIV. The first two main assumptions are stated at the end of the first paragraph of section 4 and the third main one is given in the same section and concerns our estimate of the divergence of the energy flux. The interpretations of the results in sections 5 and 6 depend on these assumptions.

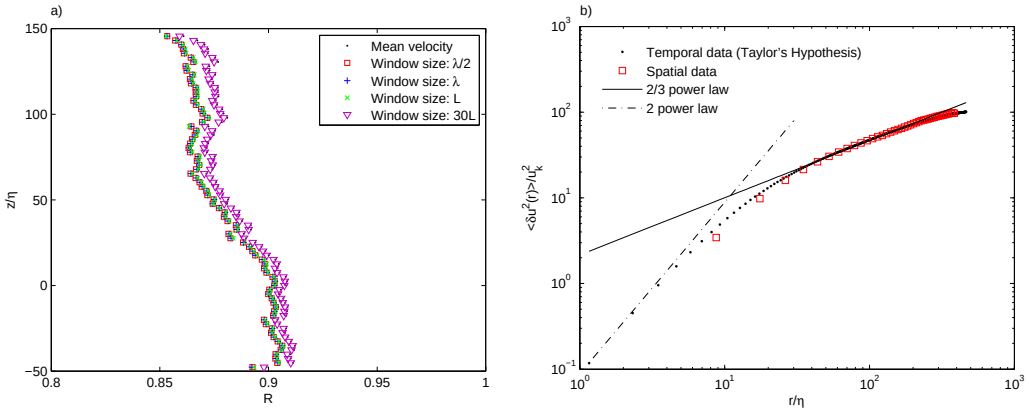

FIGURE 25. Validation of Taylor's hypothesis at x/x_*^{peak}=0.44: a) correlation coefficient between $\partial u/\partial x$ and $\partial u^d/\partial x$ for several averaging window sizes and b) second order structure function calculated with spatial and temporal (by Taylor's hypothesis) data.

Appendix A. Taylor's hypothesis validation

The main results from the present paper assume that Taylor's hypothesis is valid in the production region of the flow and are mainly focused in the location x/x_*^{peak}=0.44. In order to assess the validity of this hypothesis at this station we present some indicators based on the SFV and the LFV.

The SFV is composed by 1280 × 64 pixels (see table 4) which translates into 80 × 3 vectors, in the z and x directions, respectively. The spatial derivatives ($\partial u/\partial x$) are calculated using a second order difference scheme with the first and third vectors at each row. The derivatives computed using Taylor's hypothesis use the temporal information of the second vector and the following expression:

$$\frac{\partial u^d(z)}{\partial x} = \frac{-1}{U(z)} \frac{\partial u(z)}{\partial t} \tag{A 1}$$

where $U(z)$ is the mean velocity averaged through time information. Figure 25a shows the correlation coefficient between the aforementioned gradients along the z direction in the centreline. In an attempt to improve the correlation, the convection velocity used in equation A 1 ($U(z)$) is computed using the local mean velocity (usual procedure when applying Taylor's hypothesis) or using a local averaging window in the temporal data with different sizes namely $\lambda/2$ (where λ is the Taylor microscale), λ, L (L is the integral length scale of u in the x direction) and $30L$. The use of local windows proved to capture better the derivative of strong events but it is not as effective in capturing the weaker ones resulting in a slight loss of the overall correlation. Nevertheless, the level of correlation is in line with what other authors reported such as Ganapathisubramani *et al.* (2007) and Gomes-Fernandes *et al.* (2014) and Taylor's hypothesis is applied using a global mean velocity as the convection velocity.

Figure 25b shows the second order structure function $< \delta u^2(r) >$ at the centreline in x/x_*^{peak}=0.44 calculated using temporal data and Taylor's hypothesis and spatial data. The spatial data is computed using the LFV which is 100 × 180 mm^2 and the statistics are converged with 5 runs of 8126 vector fields each. In the spatial data the centreline at x/x_*^{peak}=0.44 is kept as the centroid and $< \delta u^2(r) >$ is computed between points

equidistant from this point in the x direction. The agreement between the two methods is good which indicates that Taylor's hypothesis is valid in this region.

REFERENCES

Batchelor, G. K. 1953 *The Theory of Homogeneous Turbulence*. Cambridge Univ. Press., Cambridge.

Braza, M., Perrin, R. & Hoarau, Y. 2006 Turbulence properties in the cylinder wake at high reynolds numbers. *Journal of Fluids and Structures* **22** (6), 757–771.

Danaila, L., Krawczynski, J. F., Thiesset, F. & Renou, B. 2012 Yaglom-like equation in axisymmetric anisotropic turbulence. *Physica D* **241** (3), 216–223.

Deissler, R. G. 1961 Effects of inhomogeneity and of shear flow in weak turbulent fields. *Phys. Fluids* **4** (10), 1187.

Discetti, S., Ziskin, I. B., Astarita, T., Adrian, R. J. & Prestridge, K. P. 2013 PIV measurements of anisotropy and inhomogeneity in decaying fractal generated turbulence. *Fluid Dynamics Research* **45** (6), 061401.

Dong, S., Karniadakis, G. E., Ekmekci, A. & Rockwell, D. 2006 A combined direct numerical simulation–particle image velocimetry study of the turbulent near wake. *J. Fluid Mech.* **569** (1), 185–207.

Ganapathisubramani, B., Lakshminarasimhan, K. & Clemens, N. T. 2007 Determination of complete velocity gradient tensor by using cinematographic stereoscopic PIV in a turbulent jet. *Exp. Fluids* **42**, 923–939.

Gomes-Fernandes, R., Ganapathisubramani, B. & Vassilicos, J. C. 2012 Particle image velocimetry study of fractal-generated turbulence. *J. Fluid Mech.* **711**, 306–336.

Gomes-Fernandes, R., Ganapathisubramani, B. & Vassilicos, J. C. 2014 Evolution of the velocity-gradient tensor in a spatially developing turbulent flow. *J. Fluid Mech.* **756**, 252–292.

Hill, R. J. 2002 Exact second-order structure-function relationships. *J. Fluid Mech.* **468**, 317–326.

Hurst, D. & Vassilicos, J. C. 2007 Scalings and decay of fractal-generated turbulence. *Phys. Fluids* **19** (035103).

Jayesh & Warhaft, Z. 1992 Probability distribution, conditional dissipation, and transport of passive temperature fluctuations in grid-generated turbulence. *Phys. Fluids A* **4**, 2292–2307.

Kolmogorov, A. N. 1941*a* Dissipation of energy in locally isotropic turbulence. *C.R. Akad Sci. SSSR* **32**, 16–18.

Kolmogorov, A. N. 1941*b* The local structure of turbulence in incompressible viscous fluid for very large reynolds numbers. *C.R. Akad Sci. SSSR* **30**, 301–305.

Kolmogorov, A. N. 1941*c* On degeneration of isotropic turbulence in an incompressible viscous liquid. *C.R. Akad Sci. SSSR* **31**, 538–540.

Laizet, S. & Vassilicos, J. C. 2011 DNS of fractal-generated turbulence. *Flow, Turbulence and Combustion* **87**, 673–705.

Laizet, S. & Vassilicos, J. C. 2012 Fractal space-scale unfolding mechanism for energy-efficient turbulent mixing. *Phys. Rev. E* **86** (4), 046302.

Laizet, S. & Vassilicos, J. C. 2015 Stirring and scalar transfer by grid-generated turbulence in the presence of a mean scalar gradient. *J. Fluid Mech.* **764**, 52–75.

Laizet, S., Vassilicos, J. C. & Cambon, C. 2013 Interscale energy transfer in decaying turbulence and vorticity-strain rate dynamics in grid-generated turbulence. *Fluid Dynamics Research* **45** (6), 061408.

Lamriben, C., Cortet, P.-P. & Moisy, F. 2011 Direct measurements of anisotropic energy transfers in a rotating turbulence experiment. *Phys. Rev. Lett.* **107** (2), 024503.

Marati, N., Casciola, C. M. & Piva, R. 2004 Energy cascade and spatial fluxes in wall turbulence. *J. Fluid Mech.* **521**, 191–215.

Mazellier, N. & Vassilicos, J. C. 2010 Turbulence without Richardson-Kolmogorov cascade. *Phys. Fluids* **22** (075101).

Nagata, K., Sakai, Y., Suzuki, H., Suzuki, H., Terashima, O. & Inaba, T. 2013 Tur-

bulence structure and turbulence kinetic energy transport in multiscale/fractal-generated turbulence. *Phys. Fluids* **25** (065102).

Nie, Q. & Tanveer, S. 1999 A note on third-order structure functions in turbulence. *Proc. Roy. Soc. A* **455** (1985), 1615–1635.

Richardson, L. F. 1922 *Weather prediction by numerical process*. Cambridge University Press.

Seoud, R. E. & Vassilicos, J. C. 2007 Dissipation and decay of fractal-generated turbulence. *Phys. Fluids* **19** (105108).

Soloff, S. M., Adrian, R. J. & Liu, Z-C. 1997 Distortion compensation for generalized stereoscopic particle image velocimetry. *Meas. Sci. Technol.* **8**, 1441–1454.

Tanaka, T. & Eaton, J. K. 2007 A correction method for measuring turbulence kinetic energy dissipation rate by PIV. *Exp. Fluids* **42**, 893–902.

Valente, P. C. & Vassilicos, J. C. 2011 The decay of turbulence generated by a class of multi-scale grids. *J. Fluid Mech.* **687**, 300–340.

Valente, P. C. & Vassilicos, J. C. 2014 The non-equilibrium region of grid-generated decaying turbulence. *J. Fluid Mech.* **744**, 5–37.

Valente, P. C. & Vassilicos, J. C. 2015 The energy cascade in grid-generated non-equilibrium decaying turbulence. *Phys. Fluids Under review*.